Memoirs of the Faculty of Science, Kyoto University, Series of Physics, Astrophysics, Geophysics and Chemistry, Vol. XXXVI, No. 2, Article 4, 1982

SYSTEMATIC STUDY ON THE ELASTIC SCATTERING OF 65 MEV POLARIZED PROTONS

By

Harutaka SAKAGUCHI

Department of Physics, Kyoto University, Kyoto 606, Japan

(*Received October 15, 1981*)

ABSTRACT

Elastic scattering of 65 MeV polarized protons from 25 nuclei (^{16}O-^{209}Bi) has been measured. Systematics of the optical potential, which reproduces both the analyzing power and the differential cross section data remarkably, was persued. The volume integral of the real central part of the optical potential (J_R) shows a behavior similar to the binding energy curve for the target mass number. The mean square radius of the real central part of the optical potential is found to obey the relation $\langle r^2\rangle_{pot} = (0.937\pm0.012)A^{2/3} + (6.42\pm0.21)$ fm^2. By comparing with the systematics of the charge distributions obtained from electron scattering data, it is found that the effective two-body interaction range between an incident proton and a nucleon in the target has a target mass number dependence given by $\langle r^2\rangle_{int} = (0.132\pm0.013)A^{2/3} + (4.24\pm0.24)$ fm^2. Assuming this relation, root mean square radii of the point nucleon distributions are obtained. The dependences of the J_R-value and the $\langle r^2\rangle_{pot}$-value on the mass number and energy obtained here are compared critically with recent microscopic optical potential calculations.

CONTENTS

1. Introduction

Recent progress in nuclear matter theories has made it possible to understand the nuclear optical potential microscopically in terms of a two-body nucleon-nucleon interaction. Jeukenne, Lejeune and Mahaux (JLM)[1)~4)] at Liege and Brieva and Rook[5)~9)] at Oxford have calculated the nuclear optical potential microscopically. In order to check critically these global optical potential theories and to extract new aspects in many body problems, it is necessary to measure accurately proton elastic scattering over a wide range of target nuclei and over a wide range of energies relative to the Fermi energy. In applying nuclear matter theory to scattering problems there are many difficulties to overcome by using suitable approximations. The most ambiguous process among them is the transformation procedure from infinite nuclear matter to finite nuclei such as the process using the local density approximation (LDA). As was already pointed out by Wong[10)] and Negele,[11)] the LDA is not accurate in the nuclear surface region. On the other hand, the nuclear surface is the region most sensitively explored by nuclear scattering, and surface effects will be exemplified by their mass number dependence. In order to clarify the role of the nuclear surface and to check the approximation used in the theory, it is important to determine accurately the mass number dependence of the optical potential. For the LDA, energy dependence of the t-matrix in nuclear matter is reflected directly in the potential depth. But in the folding potential of Brieva and Rook the situation is not so straightforward as in the LDA. For checking the validity of their approximation, the energy dependence of the optical potential will be a useful guide.

On the experimental side, the study of the optical potential has progressed after Becchetti and Greenless's[12)] work. If we plot the data available on elastic scattering in a two dimensional plane of incident proton energy versus target mass number, we notice that data are concentrated at energies below 35 MeV and for targets near magic nuclei. In addition, systematic experimental studies on the optical potential using a polarized proton beam are still scarce. Recently Fabrici et al. reported[13)~14)] measurements of the elastic scattering at several proton energies between 20 MeV and 45 MeV. Although their sytematic analysis utilized polarization data only partially, it has clarified the energy dependence in that region. In the intermediate energy region a group at Indiana Univ. is investigating[15)~17)] the systematics of the optical potential in a relativistic framework. In this paper we report systematic measurements on elastic scattering of polarized protons and an analysis of data over a wide range of target mass numbers, from ^{16}O to ^{209}Bi, at an incident proton energy of 65 MeV. Partial results have been published.[18)~20)] The use of high-purity germanium (HP-Ge) detectors has made possible rapid data aquisition at this energy. The 65 MeV data are thought to be valuable not only because they fill a gap in experimental data but also because of the simplicity of the reaction mechanism; they are relatively free from the giant resonance effects and the multi-step processes observed in the lower energy region.

2. Experimental method

The polarized proton beam (of 10 keV energy) from the atomic beam type polarized ion source[21] (PIS) is injected axially into the Research Center for Nuclear Physics (RCNP) Osaka Univ. AVF cyclotron.[22] A beam buncher in the injection system intensifies the beam current by about a factor of 3. The extracted beam of 65 MeV was energy analyzed and transported to the polarization experiment area.[23] As shown in Fig. 1, the beam was first focused on a target to a beam spot size of about $1\times2\ \mathrm{mm}^2$. After passing through the target, the polarized beam was again focused on a polarimeter target foil and then collected by a Faraday cup located downstream of the polarimenter. The beam current was monitored by a current digitizer whose output pulses were routed by a spin controller[24], depending on the beam polarization direction.

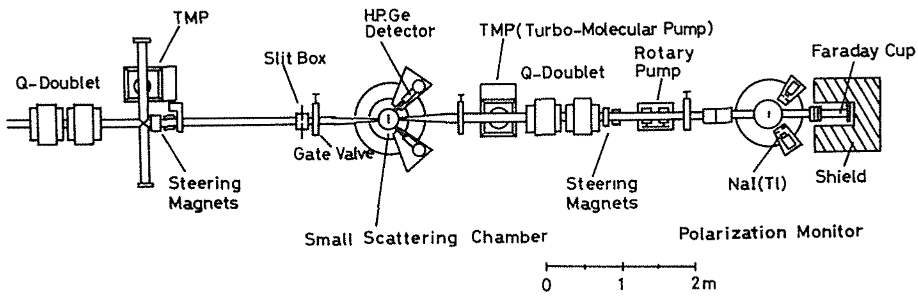

Fig. 1. A layout of the polarization experiment area.

Scattered protons were detected by 1.5 cm thick HP-Ge detectors, which were located at symmetric scattering angle to the left and right of the beam on the goniometers outside the scattering chamber. In the angle region of rapidly changing angular distributions, the detectors were placed at a distance of more than 30 cm from the scattering chamber (of 26.6 cm diameter) to obtain better angular resolution. A vacuum bag was inserted between the scattering chamber and the HP-Ge cryostat to reduce the energy loss and range straggling of the scattered particles in air. For solid targets, the acceptance solid angles of the detector were 0.1453 msr at forward angles ($\theta<32.5°$) and 0.6902 msr at backward angles ($\theta\geq32.5°$). For gas targets the vacuum bag was inserted between the front and back slits of a double-slit collimator. The gas target G-factors of the slit system were 1.09×10^{-4} at the forward angles and 2.15×10^{-4} at the backward angles. The beam direction was determined by two methods. One was the conventional kinematical crossover method. The other was to search for the scattering angles on both sides of the beam direction at which the analyzing power of $p+{}^{208}Pb$

elastic scattering changes sign rapidly. The uncertainty of the scattering angles was estimated to be less than 0.05 degrees.

The degree of beam polarization changes depending on the vacuum in the ionizer region of the PIS, the out-gassing history of the ionizer, and on other ionizer conditions. So the beam polarization was monitored continuously by a polarimeter located downstream of the scattering chamber. Scattered protons from the polarimeter target foil (a stacked 3 mg/cm^2 thick polyethylene foil) were detected by NaI(Tl) scintillators placed at the $\theta_{LAB} = 47.5$ degrees. The left-right asymmetry of the elastic scattering from ^{12}C was used to deduce the beam polarization. The polarimeter target foil was changed after an appropriate beam irradiation in order to reduce the effect of contaminant buildup. The beam polarization error due to the contaminant peak was estimated to be less than 0.2%. As the analyzing power of the ^{12}C polarimeter at $\theta_{LAB} = 47.5°$, we adopted a value of 0.975 ± 0.011, which was obtained in the double scattering experiment at $E_p = 65$ MeV by Kato et al.[25] The direction of the proton spin was reversed after every 200 pC of integrated beam charge by reversing the solenoid magnetic field direction at the inonizer of the PIS. In the later stage of the experiment the spin direction was reversed every 1 s by alternating the atomic beam rf transition mode between the weak field and strong field transition. Signals from a microprocessor triggered the spin controller which controlled the rf transition mode, the scalers, and the data storage locations in the memory of the pulse height

Table 1. Targets

Nucleus	Form	Thickness (mg/cm^2)	Enrichment
^{16}O	gas (O_2)	1-2 atm	natural (99.8%)
^{20}Ne	gas (Ne)	1-2 atm	natural (90.51%)
^{24}Mg	metal foil	3.18	99.94%
^{28}Si	metal foil	2.98	natural (92.21%)
^{40}Ar	gas (Ar)	1-2 atm	natural (99.60%)
^{40}Ca	metal foil	2.19	natural (96.97%)
^{44}Ca	metal foil	2.78	98.55%
^{48}Ca	$CaCO_3$+mylar	1.34	97.27%
^{46}Ti	metal foil	0.52	81.20%
^{48}Ti	metal foil	0.99	99.25%
^{50}Ti	metal foil	0.82	83.2%
^{54}Fe	metal foil	1.57	96.81%
^{56}Fe	metal foil	1.02	99.93%
^{59}Co	metal foil	2.09	99.83%
^{58}Ni	metal foil	2.04	99.83%
^{60}Ni	metal foil	2.04	99.79%
^{62}Ni	metal foil	1.71	96.48%
^{64}Ni	metal foil	3.55	96.48%
^{89}Y	metal foil	1.376	natural (100%)
^{90}Zr	metal foil	2.672	97.65%
^{98}Mo	metal foil	0.900	97.01%
^{100}Mo	metal foil	0.372	97.27%
^{144}Sm	metal foil	1.71	96.33%
^{208}Pb	metal foil	15.1	99.14%
^{209}Bi	metal foil	4.23	natural (100%)

analyzer, where energy spectra were stored in different memory locations depending on the polarization direction. The average beam intensity during the measurements was about 30 nA and the beam polarization was about 60–70%. The overall energy resolution detected by the HP-Ge system was 180keV–250 keV FWHM, including the beam energy spread and the range straggling due to window foils of the scattering chamber, the vacuum bag, and the HP-Ge cryostat. Table 1 lists the forms, thicknesses and enrichments of the target foils used. The thicknesses of the solid target folils were measured by dividing the total weight by the area, and for gas targets the gas pressure was monitored using a strain gauge sensor.

3. Data reduction

Analyzing powers were measured by the left and right detectors located at the same scattering angle. We denote by $L\uparrow$ the number of particles detected by the left detector in the spin up mode. $L\downarrow$, $R\uparrow$, and $R\downarrow$ are defined in an analogous way. The analyzing power $A_y(\theta)$ and its statistical error $\delta A_y(\theta)$ are calculated as follows

$$A_y(\theta)=\frac{1}{P_{\text{Beam}}}\left(\frac{r-1}{r+1}\right), \quad r\equiv\left(\frac{L\uparrow\cdot R\downarrow}{L\downarrow\cdot R\uparrow}\right)^{1/2}$$

$$P_{\text{Beam}}=\frac{1}{A_y(^{12}C)}\left(\frac{r'-1}{r'+1}\right), \quad r'\equiv\left(\frac{L\uparrow_{\text{pol}}\cdot R\downarrow_{\text{pol}}}{L\downarrow_{\text{pol}}\cdot R\uparrow_{\text{pol}}}\right)^{1/2}$$

$$\delta A_y(\theta)=A_y(\theta)\left[\left(\frac{\delta P_{\text{Beam}}}{P_{\text{Beam}}}\right)^2+\left(\frac{\delta A}{A}\right)^2\right]^{1/2}$$

$$=A_y(\theta)\left[\left(\frac{\delta P_{\text{Beam}}}{P_{\text{Beam}}}\right)^2+\left(\frac{r}{r^2-1}\right)^2\left(\frac{1}{R\uparrow}+\frac{1}{R\downarrow}+\frac{1}{L\uparrow}+\frac{1}{L\downarrow}\right)\right]^{1/2}$$

$$\delta P_{\text{Beam}}=P_{\text{Beam}}(\theta)\left[\left(\frac{\delta A_y(^{12}C)}{A_y(^{12}C)}\right)^2+\left(\frac{r'}{r'^2-1}\right)^2\left(\frac{1}{R\uparrow_{\text{pol}}}+\frac{1}{R\downarrow_{\text{pol}}}+\frac{1}{L\uparrow_{\text{pol}}}+\frac{1}{L\downarrow_{\text{pol}}}\right)\right]^{1/2}$$

$$A_y(^{12}C)=0.975 \qquad \delta A_y(^{12}C)=0.011$$

where $L\uparrow_{\text{pol}}$ denotes carbon elastic peak sum for the left polarimeter detector in the spin up mode, and $L\downarrow_{\text{pol}}$, $R\uparrow_{\text{pol}}$, and $R\downarrow_{\text{pol}}$ are similarly defined. $A_y(^{12}C)$ and $\delta A_y(^{12}C)$ are the carbon analyzing power and its uncertainty at the scattering angle $\theta_{\text{LAB}}=47.5°$ and $E_p=65$ MeV. Differential cross section data were corrected by the detector efficiency due to the nuclear reaction in the HP-Ge itself. Energy dependent detector efficiency $\varepsilon(E_p)$ in the energy region of 45 MeV to 65 MeV is obtained from the Makino's data[26] according to the relation

$$\varepsilon(E)=1.0267-0.0011333E$$

Using this formula, the difference of the elastic peak detecting efficiency between $\theta_{\mathrm{LAB}}=0°$ and $\theta_{\mathrm{LAB}}=80°$ was 0.7% for ^{16}O and 0.3% for ^{40}Ca. Thus the correction due to Makino's data affected the relative angular distributions of the differential cross sections negligibly. Measured cross section and analyzing power data are plotted in Fig. 2. Numerical values of the data are listed in the Appendix. Error bars shown in the figure and the Appendix are only the statistical ones. In the analyzing power data, uncertainties of the ^{12}C-polarimeter analyzing power are included. We notice a systematic shift of the diffraction pattern as the target mass number increases. In particular, a sharp rise near 30° in the analysing power data shifts forwards as the target mass number increases.

4. Optical potential fitting

The optical potential fitting to the measured data was performed using the automatic search code MAGALI of Raynal.[27]

The following optical potential was as used;

$$U(r)=V_{\mathrm{Coul}}(r)-V_r f(r;r_R,a_R)-iW_v f(r;r_{wv},a_{wv})$$
$$+4a_{ws}\boldsymbol{W_s i}\frac{d}{dr}f(r;r_{ws},a_{ws})$$
$$+V_{ls}\left(\frac{\hbar}{m_\pi c}\right)^2\left(\frac{1}{r}\frac{d}{dr}f(r;r_{ls},a_{ls})\right)(\boldsymbol{\sigma}\cdot\boldsymbol{L})$$

where

$$f(r;r_0,a_0)=(1+\exp((r-r_0A^{1/3})/a_0))^{-1}$$

$$V_{\mathrm{Coul}}(r)=\begin{cases}\dfrac{Ze^2}{2r_cA^{1/3}}\left(3-\dfrac{r^2}{r_c^2A^{2/3}}\right) & r\leq r_cA^{1/3}\\[2ex] \dfrac{Ze^2}{r} & r\geq r_cA^{1/3}\end{cases}$$

A search for best-fit values of the optical potential parameters was started using the gas-target data. The probability of becoming trapped in a false local minimum during the search for a χ^2-minimum was thought to be small, since uncertainties in the cross section due to uncertainties in the target thickness measurement are small for the gas targets. For ^{40}Ar, we started with the Becchetti and Greelees parameter values. The initial parameter values for ^{16}O, ^{20}Ne were obtained from the best-fit ^{40}Ar parameter set. For other targets, potential parameters of the neighbouring target which had already been fitted were adopted as a starting set. Also, a renormalization of the calculation was introduced because of the target thickness uncertainty. In Fig. 2 measured differential cross sections and analyzing powers are shown together with the best-fit optical potential calculations. The optical potential parameters and the associated χ^2-values obtained are listed in Table 2.

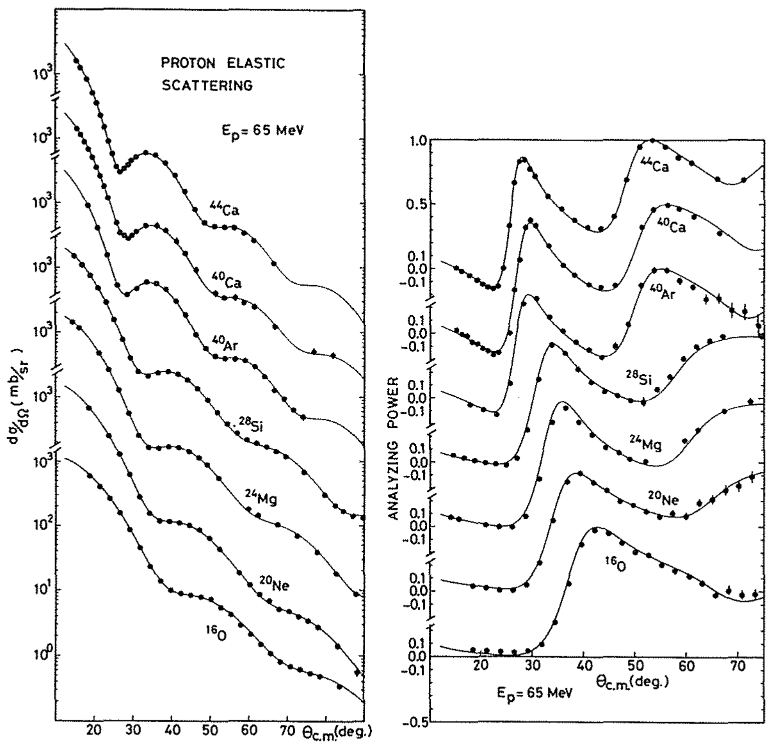

Fig. 2. (a) Measured cross sections and analyzing powers. The solid curves are optical potential calculations. The parameters used are listed in Table 2. In fitting the analyzing power data, the data used were extended to $\theta_{cm}=90°$ for the light nuclei although only the data ($\theta_{cm} \leq 75°$) are shown in the figure.

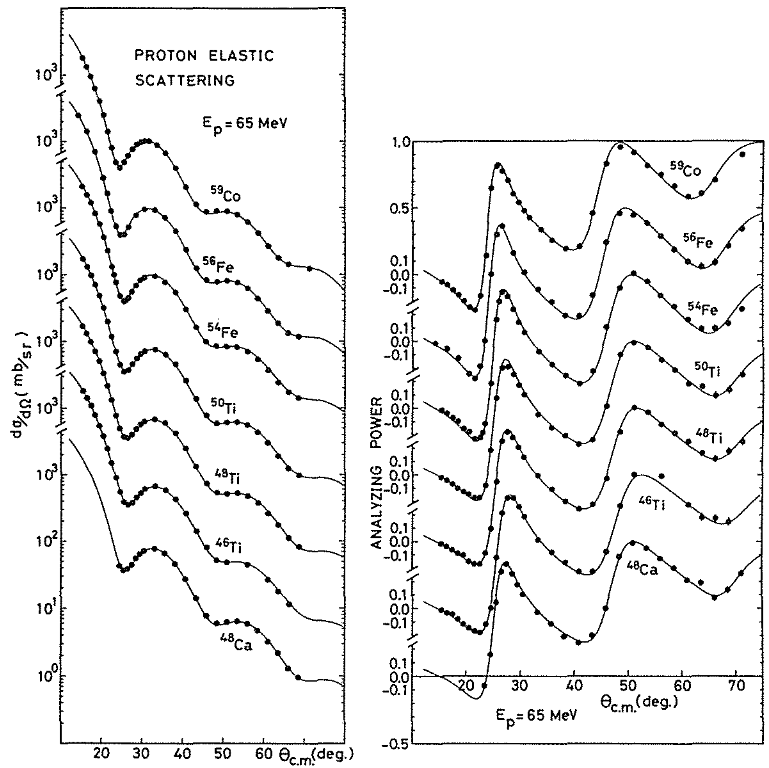

Fig. 2. (b) Measured cross sections and analyzing powers. The solid curves are optical potential calculations. The parameters used are listed in Table 2.

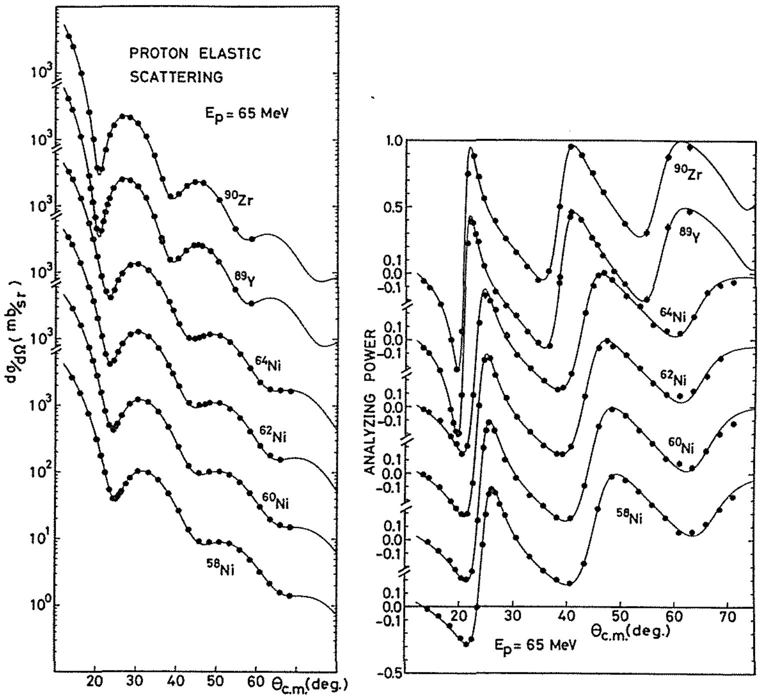

Fig. 2. (c) Measured cross sections and analyzing powers. The solid curves are optical potential calculations. The parameters used are listed in Table 2.

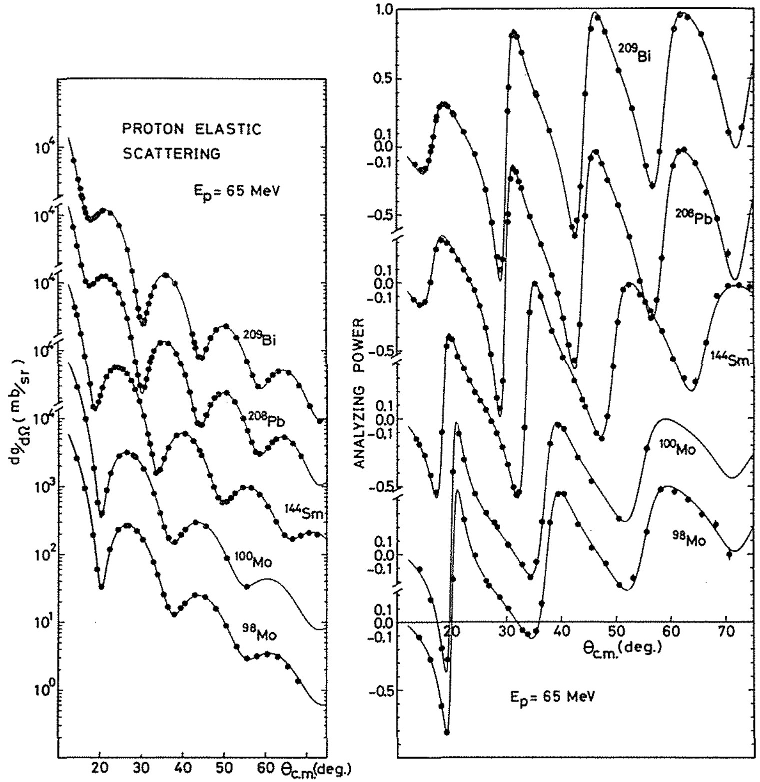

Fig. 2. (d) Measured cross sections and analyzing powers. The solid curves are optical potential calculations. The parameters used are listed in Table 2.

Table 2. Best fit optical potential parameters Coulomb radius is fixed to $r_c=1.25$ fm.

Nucleus	V_R	r_R	a_R	W_v	r_{wv}	a_{wv}	W_s	r_{ws}	a_{ws}	V_{LS}	r_{LS}	a_{LS}	χ^2/F	Renorm. Factor
^{16}O	27.172	1.297	0.6556	12.847	0.2762	1.198	3.290	1.350	0.375	5.793	1.057	0.5807	1.50	1.04
^{20}Ne	31.162	1.212	0.7439	7.709	0.9552	0.9484	2.658	1.320	0.5367	5.402	1.015	0.6860	1.25	1.05
^{24}Mg	27.242	1.251	0.6864	10.525	0.8908	1.041	1.809	1.395	0.3850	5.269	1.022	0.6364	2.29	1.23
^{28}Si	33.912	1.176	0.7248	9.917	0.8388	0.3660	5.348	1.241	0.5656	5.970	1.007	0.6181	1.68	1.05
^{40}Ar	34.249	1.208	0.7266	9.063	1.137	0.7498	2.897	1.357	0.4928	5.606	1.061	0.6722	1.64	1.07
^{40}Ca	33.285	1.232	0.7080	8.131	1.164	0.7993	2.737	1.344	0.4413	5.796	1.088	0.6317	0.806	0.807
^{44}Ca	31.474	1.246	0.7007	9.703	1.120	0.9099	2.553	1.329	0.4476	5.449	1.094	0.6554	1.16	0.956
^{48}Ca	32.907	1.230	0.6808	10.228	1.187	0.7824	2.515	1.344	0.3975	5.680	1.091	0.6475	0.792	1.03
^{46}Ti	31.691	1.241	0.7082	8.034	1.182	0.8090	2.376	1.347	0.4949	5.285	1.094	0.6554	0.772	1.03
^{48}Ti	31.425	1.242	0.7041	8.244	1.191	0.8346	2.189	1.349	0.4199	5.209	1.094	0.6554	0.608	0.955
^{50}Ti	32.610	1.226	0.6898	9.521	1.162	0.8216	2.506	1.346	0.3941	5.248	1.083	0.6276	0.550	0.982
^{54}Fe	33.195	1.212	0.6907	10.410	1.047	0.7670	2.922	1.330	0.4803	5.608	1.071	0.6155	0.550	1.11
^{56}Fe	34.870	1.197	0.7138	11.354	1.004	0.8162	3.333	1.316	0.5307	5.581	1.051	0.6285	0.678	1.01
^{59}Co	33.634	1.212	0.7177	9.606	1.133	0.8240	2.231	1.346	0.4654	5.559	1.071	0.6554	0.610	0.966
^{58}Ni	35.466	1.173	0.7248	12.499	0.9729	0.6262	3.618	1.319	0.5639	5.907	1.027	0.6554	0.511	1.08
^{60}Ni	34.812	1.195	0.7171	11.662	1.001	0.8083	3.282	1.317	0.5345	5.781	1.049	0.6554	0.439	1.11
^{62}Ni	33.831	1.218	0.7175	11.356	1.052	0.8815	3.195	1.320	0.4562	5.757	1.074	0.6554	0.638	1.04
^{64}Ni	33.858	1.209	0.7234	11.518	1.019	0.7744	3.864	1.310	0.5422	5.822	1.063	0.6554	0.696	1.02
^{89}Y	35.463	1.232	0.7084	8.545	1.274	0.7226	2.806	1.301	0.3847	5.506	1.147	0.6300	0.918	1.06
^{90}Zr	34.861	1.233	0.7129	9.230	1.223	0.7070	2.621	1.352	0.4180	5.395	1.138	0.6527	0.498	0.936
^{98}Mo	34.460	1.240	0.7407	8.585	1.016	0.8210	5.163	1.261	0.6046	5.035	1.147	0.6603	0.729	0.951
^{100}Mo	34.933	1.244	0.7311	7.058	1.072	0.7878	5.901	1.248	0.6005	5.267	1.156	0.6339	0.283	1.08
^{144}Sm	36.162	1.230	0.7288	10.439	1.016	0.8210	5.676	1.248	0.6005	5.397	1.151	0.6224	0.584	1.10
^{208}Pb	39.105	1.223	0.7461	9.816	1.142	0.7775	5.758	1.253	0.5872	5.838	1.175	0.6103	0.652	1.13
^{209}Bi	37.399	1.229	0.7347	12.160	1.016	0.8210	6.236	1.252	0.5998	5.447	1.155	0.6330	0.696	1.09

Uncertainties in the experimental data are mainly due to inhomogenities of the target foil thickness and to the scattering angle errors (less than 0.1°) rather than to counting statistics. Therefore the uncertainties used during the parameter search were

$$\delta\left(\frac{d\sigma}{d\Omega}\right)=\mathrm{Max}\left(0.03\times\left(\frac{d\sigma}{d\Omega}\right),\left(\frac{d\sigma}{d\Omega}\right)_{\text{statistical}}\right)$$

and

$$\delta A(\theta)=\mathrm{Max}\,(0.03,\,\delta A(\theta)_{\text{statistical}})$$

in order to avoid trapping in an unphysical local χ^2-minimum. As for the data points in Fig. 2, the error bars for the cross sections include only the statistical errors, while the error bars for analyzing powers include the uncertainty of the ^{12}C-polarimeter analyzing power in addition.

5. Systematics of the mean square radius of the real central part of the optical potential and the effective interaction range

From the real central part of the optical potential obtained in this analysis, the mean square radius of the potential $\langle r^2\rangle_{\text{pot}}$, was calculated and is plotted as a function of $A^{2/3}$ (A denotes the target mass number) in Fig. 3. The $\langle r^2\rangle_{\text{pot}}$ data are remarkably linear in $A^{2/3}$. A linear least-squares fit to the $\langle r^2\rangle_{\text{pot}}$ data gives

$$\langle r^2\rangle_{\text{pot}}=(0.937\pm0.012)\,A^{2/3}+6.42\pm0.21\ \text{fm}^2\,. \tag{1}$$

The error bars in Fig. 3 indicate the uncertainties in the optical potential fitting and were calculated using the following procedure. First, all the

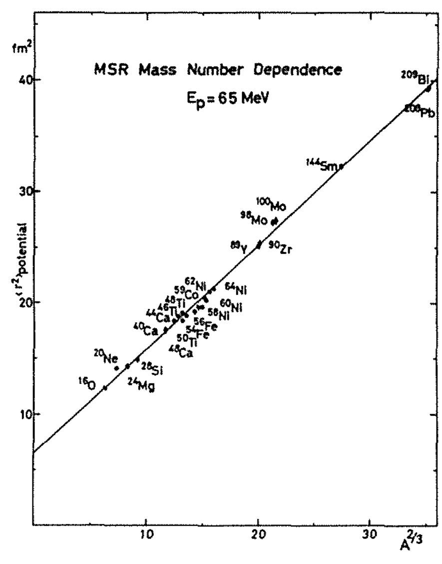

Fig. 3. Mean square radii of the real central part of the optical potentials are shown as a function of the target mass number A. The definition of the error bars in the figure is explained in the text. The numerical data with error bars are listed in Table 3. The solid line is obtained by least-quare linear fitting to the data.

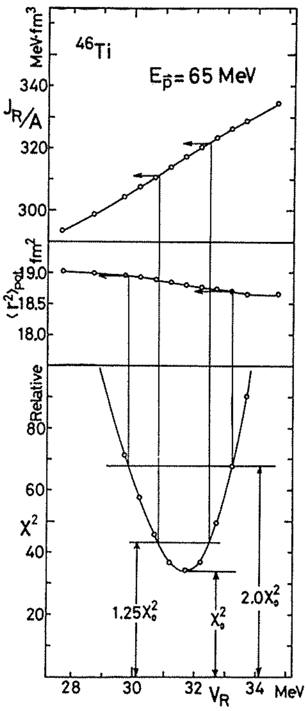

Fig. 4. An example of the procedure for deducing the error bar is shown. The volume intergral per nucleon of the real central part of the optical potential, the mean square radius of the potential and the total χ^2-value are plotted as a function of the potential depth V_R for ^{46}Ti. For $\langle r^2\rangle_{\rm rot}$, error bars are obtained from the $2\chi_0{}^2$ point and for J_R/A from 1.25 $\chi_0{}^2$ point.

parameters except V_r and r_c were searched for to obtain the $\chi^2_{\rm min}(V_r)$ as a function of V_r. A $\chi^2_{\rm min}(V_r)$ curve for ^{46}Ti case is shown in Fig. 4. The curve resembles a parabola. Then the error of $\langle r^2\rangle_{\rm pot}$ was calculated from the $\langle r^2\rangle_{\rm pot.1}$ and $\langle r^2\rangle_{\rm pot.2}$ values, which were obtained with the parameter sets at $\chi^2_{\rm min}(V_r)=2\chi^2_0$ (best fit). Thus, the uncertainty due to the well known VR^n $=$constant parameter correlation is included in the error bars.

The linear relation between $\langle r^2\rangle_{\rm pot}$ and $A^{2/3}$ is understood by using a simple folding model. As was shown already by Greenlees, Pyle and Tang,[28] the real central part of the optical potential can be written as

$$U(\boldsymbol{r}_0)=\int\rho(\boldsymbol{r})V_{\rm int}(|\boldsymbol{r}-\boldsymbol{r}_0|)\,d\boldsymbol{r}^3\,, \tag{2}$$

where $\rho(\boldsymbol{r})$ is the density distribution of point nucleons and $V_{\rm int}(r)$ is an effective two body interaction. For a nucleus with a rotationally symmetric density distribution, the mean square radius of the potential deduced from Eq. (2) is

$$\langle r^2\rangle_{\rm pot}=\langle r^2\rangle_{\rm matt}+\langle r^2\rangle_{\rm int}\,, \tag{3}$$

where $\langle r^2\rangle_{\rm pot}=\int r^2U(\boldsymbol{r})\,{\rm d}\boldsymbol{r}^3/\int U(\boldsymbol{r})\,{\rm d}\boldsymbol{r}^3$, $\langle r^2\rangle_{\rm matt}=\int r^2\rho(\boldsymbol{r})\,{\rm d}\boldsymbol{r}^3/\int\rho(\boldsymbol{r})\,{\rm d}\boldsymbol{r}^3$ and $\langle r^2\rangle_{\rm int}=\int r^2V_{\rm int}(r)\,{\rm d}\boldsymbol{r}^3/\int V_{\rm int}(r)\,{\rm d}\boldsymbol{r}^3$. If we assume that $U(\boldsymbol{r})$ and $\rho(\boldsymbol{r})$ are sphrically symmetric Fermi functions, $\langle r^2\rangle_{\rm matt}$ can be calculated in a good approximation[29),30)] as

$$\langle r^2\rangle_{\text{matt}}=\frac{3}{5}R_m{}^2+\frac{7}{5}\pi^2a_m{}^2\,, \tag{4}$$

where R_m and a_m are the half density radius and diffuseness of the point nucleon density distribution, respectively. Therefore $\langle r^2\rangle_{\text{pot}}$ is expressed as

$$\langle r^2\rangle_{\text{pot}}=\frac{3}{5}R_m{}^2+\frac{7}{5}\pi^2a_m{}^2+\langle r^2\rangle_{\text{int}}\,. \tag{5}$$

In order to obtain a relation between the half density radius and the mass number, we use the volume integral of the Fermi-type density distribution:

$$\int\rho(r)\,d\boldsymbol{r}^3=\frac{4\pi}{3}R_m{}^3\left(1+\frac{\pi^2a_m{}^2}{R_m{}^2}\right)\rho_0=A \tag{6}$$

where

$$\rho(r)=\frac{\rho_0}{1+\exp\left(\dfrac{r-R_m}{a_m}\right)}$$

Since a_m and ρ_0 are reasonably constant with A, the half density radius R_m is calculated as a function of A, as

$$R_m=r_mA^{1/3}\left\{1-\frac{1}{3}\left(\frac{\pi^2a_m{}^2}{r_m{}^2A^{2/3}}\right)+\frac{1}{81}\left(\frac{\pi^2a_m{}^2}{r_m{}^2A^{2/3}}\right)^3+\cdots\right\} \tag{7}$$

where

$$r_m=\left(\frac{3}{4\pi\rho_0}\right)^{1/3}$$

Inserting (7) into (5), we obtain for $\langle r^2\rangle_{\text{pot}}$,

$$\langle r^2\rangle_{\text{pot}}=\langle r^2\rangle_{\text{int}}+\frac{3}{5}r_m{}^2A^{2/3}+\pi^2a_m{}^2+\frac{1}{15}\pi^2a_m{}^2\left(\frac{\pi^2a_m{}^2}{r_m^2A^{2/3}}\right)+\cdots \tag{8}$$

The 4th term can be neglected, since the ratio of the 4th term to the 3rd term is less than 0.02 for nuclei considered ($A\geq 16$). We finally obtain an approximate relation

$$\langle r^2\rangle_{\text{pot}}=\frac{3}{5}r_m{}^2A^{2/3}+\pi^2a_m{}^2+\langle r^2\rangle_{\text{int}}\,. \tag{9}$$

If we treat $\langle r^2\rangle_{\text{int}}$ as a constant value as usual, $\langle r^2\rangle_{\text{pot}}$ is linear in $A^{2/3}$ with the coefficient $\frac{3}{5}r_m{}^2$. In order to obtain the $\langle r^2\rangle_{\text{int}}$-value, we need to know the a_m-value, which is inferred from the charge distribution data. By comparing the two linear relations (1) and (9), we obtain the value of $r_m = (1.25\pm 0.01)$ fm.

If we assume that the point proton density distribution is also of the Fermi-type (as we did for nuclear matter distribution), then $\langle r^2\rangle_{\text{charge}}$ can be written in terms of the half-density radius R_p, the diffuseness a_p of the point proton distribution, and the mean square radius of the charge distribution of the proton itself, $\langle r^2\rangle_{\text{proton}}$, as

$$\langle r^2\rangle_{\text{charge}}=\frac{3}{5}R_p^2+\frac{7}{5}\pi^2 a_p^2+\langle r^2\rangle_{\text{proton}}\,. \tag{10}$$

For a relation between R_p and the mass number A, we use the same relation as (7)

$$R_p=r_pA^{1/3}\left\{1-\frac{1}{3}\left(\frac{\pi^2 a_p^2}{r_p^2A^{2/3}}\right)+\frac{1}{81}\left(\frac{\pi^2 a_p^2}{r_p^2A^{2/3}}\right)^3+\cdots\right\} \tag{11}$$

We finally obtain a linear relation for $\langle r^2\rangle_{\text{charge}}$ with $A^{2/3}$.

$$\langle r^2\rangle_{\text{charge}}=\frac{3}{5}r_p^2A^{2/3}+\pi^2 a_p^2+\langle r^2\rangle_{\text{proton}} \tag{12}$$

The mean square radius of the charge distribution, $\langle r^2\rangle_{\text{charge}}$, from electron scattering[31] is plotted in Fig. 5 as a function of $A^{2/3}$. By least-squares linear fitting, we obtained $\langle r^2\rangle_{\text{charge}}=(0.799\pm0.006)\,A^{2/3}+(2.50\pm0.12)$ fm^2. By introducing the $\langle r^2\rangle_{\text{proton}}=0.64$ fm^2 and comparing values from electron scattering with equation (12), we obtain $r_p=(1.154\pm0.004)$ fm and $a_p=(0.434\pm0.014)$ fm. These values are slightly modified by taking into account the

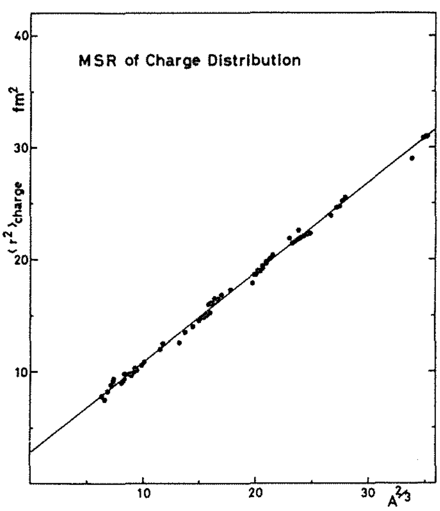

Fig. 5. Mean square radii of the charge distribution obtained from the electron scattering are plotted as a function of the mass number A.

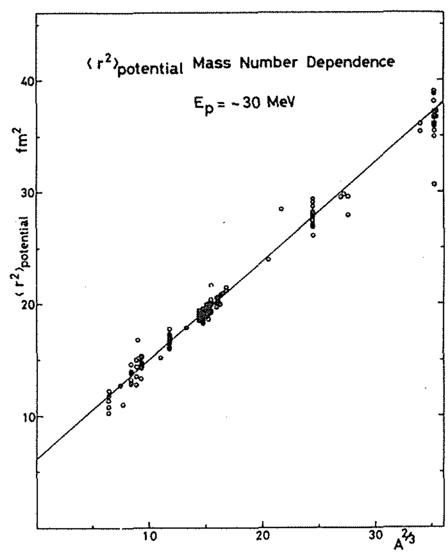

Fig. 6. Mean square radii of the real central part of the optical potentials at E_p=27-32 MeV are plotted as a function of $A^{2/3}$.

neutron charge distribution.[31] Thus $r_p = (1.158 \pm 0.004)$ fm and $a_p = (0.470 \pm 0.012)$ fm are obtained. If the diffuseness of the point nucleon distribution is assumed to be equal to the diffuseness of the point proton distribution, we get the value of $\langle r^2 \rangle_{\text{int}} = (4.24 \pm 0.24)$ fm^2.

We notice that the value of r_m extracted from the present experiment is larger than that of r_p obtained from the electron scattering data. In order to show that such a difference is common to proton scattering, linear fits were made to the mean square potential radii from Perey's collection[32] of optical potential results at 27–32 MeV and 47–52 MeV incident proton energies. These are shown in Fig. 6 and Fig. 7, respectively. The values obtained are $r_m = (1.21 \pm 0.03)$ fm and $\langle r^2 \rangle_{\text{int}} = (4.06 \pm 0.84)$ fm^2 at 30 MeV, and $r_m = (1.19 \pm 0.02)$ fm and $\langle r^2 \rangle_{\text{int}} = (4.98 \pm 0.74)$ fm^2 at 50 MeV. Although the 30 MeV data and the 50 MeV data consist of optical potential parameters by many authors and hence could contain many inconsistencies among the parameters obtained due to different fitting principles, the r_m and $\langle r^2 \rangle_{\text{int}}$ values from the 30 MeV and 50 MeV data are consistent with our values, and r_m is larger than the r_p value of 1.158 fm. From the analysis of the 800 MeV–1 GeV data, it is concluded that r_m is approximately equal to r_p.

One answer to this contradiction is to introduce a target mass number dependence into the effective interaction range $\langle r^2 \rangle_{\text{int}}$. As demonstrated in Fig. 3, the linear relation between $\langle r^2 \rangle_{\text{pot}}$ and $A^{2/3}$ is confirmed and acceptable. Therefore the mass number dependence to be introduced into $\langle r^2 \rangle_{\text{int}}$ must also be linear in $A^{2/3}$. A recent argument[34] based on experimental data and the experimental results from the Los Alamos Meson Physics Facility (LAMPF),[38)~43)] show that with a small correction from the charge distribution in the neutron itself, the difference between the root mean square

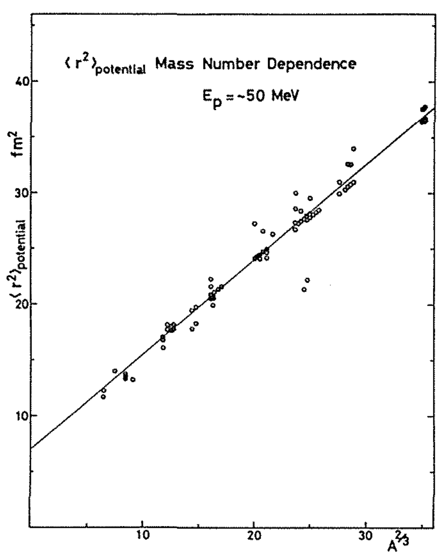

Fig. 7. Mean square radii of the real central part of the optical potentials at E_p=47–52 MeV are plotted as a functtion of $A^{2/3}$.

radius of the point nucleon distribution and that of the point proton distribution is less than 0.1 fm, which is smaller than the error in our $\langle r^2\rangle_{\rm int}$-value. Thus the average density distribution of point nucleons may be thought to be equal to that of point protons. Then the effective two-body interaction range obtained is

$$\langle r^2\rangle_{\rm int} = (0.132 \pm 0.013)\, A^{2/3} + (4.24 \pm 0.24)\ {\rm fm}^2\,.$$

According to the recent theoretical work of Brieva[9] on the nucleon-nucleus optical potential using a realistic nucleon-nucleon interaction, the exchange term is repulsive in the nuclear center, whereas at the surface it is attractive. An exchange term of this type introduces a mass number dependence of the effective interaction range, if $\langle r^2\rangle_{\rm int}$ is defined as $\langle r^2\rangle_{\rm int} = \langle r^2\rangle_{\rm pot} - \langle r^2\rangle_{\rm charge} + \langle r^2\rangle_{\rm proton}$. Another source of the mass number dependence may come from a small difference between the point proton and the point neutron distributions, because the proton-neutron interaction is stronger than the proton-proton interaction, and this fact may enhance the effect from the density distribution difference. Thus the mass number dependence of $\langle r^2\rangle_{\rm int}$ is an empirical relation and reflects various many body effects. The true origin of this mass number dependence may be explained by an elaborate microscopic calculation. The possibility of a target dependence of the effective interaction range has been suggested already by B. Sinha.[30] Our $\langle r^2\rangle_{\rm int}$-value is larger than the GPT's value[28] of (2.25 ± 0.6) fm^2. GPT's $\langle r^2\rangle_{\rm int}$-value was obtained in the search for the χ^2-minimum mainly of the cross section data because of the partial lack of polarization data at that time. By equally weighting the polarization and cross section data we were able to reduce the VR^n type ambiguity and have found a larger value for the mass number dependent $\langle r^2\rangle_{\rm int}$-value. Bertsch et al. also obtained a large $\langle r^2\rangle$-value ($\sim$6 fm^2) for inelastic scattering by fitting the interaction to the matrix element of the scattering operator, t-matrix or G-matrix. Since their interaction is effective at the nuclear surface and is not density dependent, their $\langle r^2\rangle_{\rm int}$ does not have any mass number dependence. Our $\langle r^2\rangle_{\rm int}$-values for medium weight nuclei are as large as the one obtained in the Bertsch's calculation.[44]

6. The mass number dependence of the effective two-body interaction range deduced from the optical potential for deuteron, helium-3 and alpha particles

The $\langle r^2\rangle_{\rm pot}$-values for other light ion projectiles were calculated and plotted as a function of $A^{3/2}$ in Fig. 8 for 56 MeV deuteron optical potential data,[45] in Fig. 9 for 109 MeV and 119 MeV ^{3}He[46] optical potentials and in Fig. 10 for 166 MeV alpha particles.[32] In each case the solid lines are linear fits by the least square method and are expressed

$$\langle r^2\rangle_{\rm pot} = 0.859 A^{2/3} + 8.62\ {\rm fm}^2 \qquad {\rm for} \quad E_d = 56\ {\rm MeV},$$

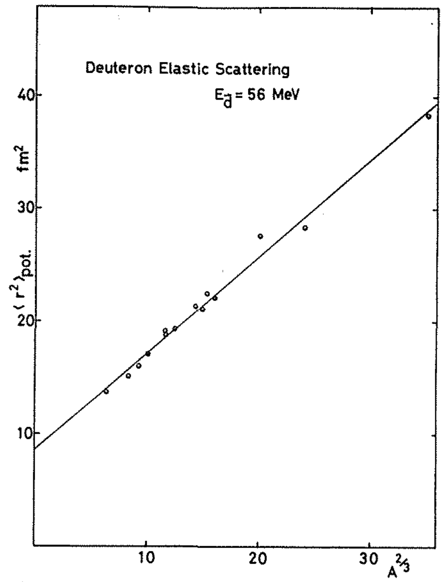

Fig. 8. Mean square radii of the real cenral part of the deuteron optical potential at E_d=56 MeV are plotted as a function of $A^{2/3}$. The solid line is a least linear fit to the data.

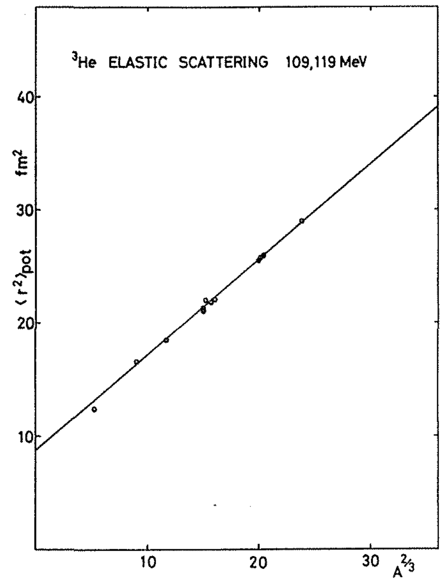

Fig. 9. Mean square radii of the real central part of the helium-3 optical potential at $E_{^3\mathrm{He}}$=109, 119 MeV are plotted as a function of $A^{2/3}$. The solid line is a least linear fit to the data.

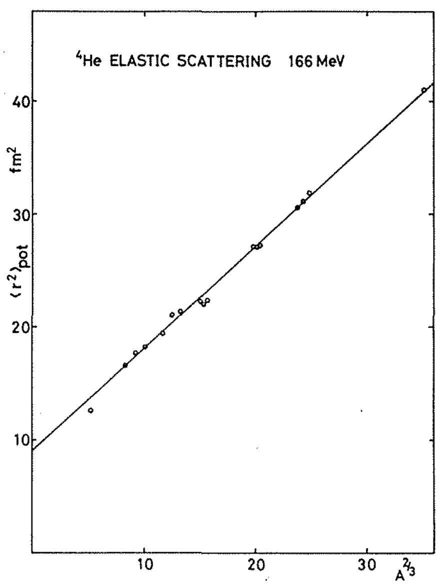

Fig. 10. Mean square radii of the real central part of the optical potential at $E_{^4\mathrm{He}}$=166 MeV are plotted as a funciion of $A^{2/3}$. The solid line is a linear fit to the data.

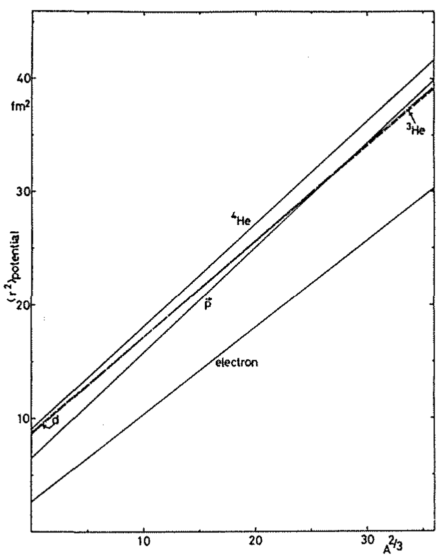

Fig. 11. Mass number dependences of the mean square radii of the real central part of the optical potential are compared with each other for p, d, ^{3}He and ^{4}He projectiles.

$$\langle r^2\rangle_{\text{pot}}=0.843A^{2/3}+8.78\ \text{fm}^2 \qquad \text{for} \quad E_{^3\text{He}}=109\ \text{MeV}\ ,\ 119\ \text{MeV}$$

and

$$\langle r^2\rangle_{\text{pot}}=0.908A^{2/3}+8.982\ \text{fm}^2 \qquad \text{for} \quad E_{\alpha}=166\ \text{MeV}\ ,$$

respectively. If we combine all of these data, we notice in Fig. 11 that the slopes of the proton and the alpha lines are similar. The mean square radius of the real central part of the composite particle is described by the double folding model as;

$$\langle r^2\rangle_{\text{pot}}=\frac{3}{5}r_m{}^2A^{2/3}+\pi^2a_m{}^2+\langle r^2\rangle_{\text{int}}+\langle r^2\rangle_m^{\text{projectile}}$$

where

$$\langle r^2\rangle_m^{\text{projectile}}=\langle r^2\rangle_{\text{charge}}^{\text{projectile}}-\langle r^2\rangle_{\text{charge}}^{\text{proton}} \qquad \text{and}$$

$\langle r^2\rangle_m^{\text{projectile}}$ means the mean square radius of the point nucleon distribution in the projectile. Thus the intersection in Fig. 11 is the sum of $\pi^2a_m{}^2+\langle r^2\rangle_m^{\text{projectile}}$ and the mass number independent part of the $\langle r^2\rangle_{\text{int}}$. The slope is the sum of $\frac{3}{5}r_m{}^2$ and the mass number dependent part of the $\langle r^2\rangle_{\text{int}}$. Using the formula above and the electron scattering data for the $\langle r^2\rangle_{\text{charge}}^{\text{projectile}}$-values. The mean square radius of the effective two-body interaction $\langle r^2\rangle_{\text{int}}$ is calculated as follows;

$$\langle r^2\rangle_{\text{int}}=(0.132A^{2/3}+4.24)\ \text{fm}^2 \qquad \text{for proton}$$

$$\langle r^2\rangle_{\text{int}}=(0.087A^{2/3}+2.45)\ \text{fm}^2 \qquad \text{for deuteron}$$

$$\langle r^2\rangle_{\text{int}}=(0.075A^{2/3}+3.84)\ \text{fm}^2 \qquad \text{for helium-3}$$

$$\langle r^2\rangle_{\text{int}}=(0.140A^{2/3}+4.89)\ \text{fm}^2 \qquad \text{for alpha}$$

These values show that for the hard projectiles such as protons and alpha particles, mass number dependence of $\langle r^2\rangle_{\text{int}}$ is large and that for the soft projectiles like deuterons and helium-3, the mass number dependences of the $\langle r^2\rangle_{\text{int}}$ and $\langle r^2\rangle_{\text{int}}$-values themselves are small.

The origin of such target mass number dependence and the projectile dependence may be in the Pauli-principle. The a $A^{2/3}+b$ type mass number dependence is divergent on A and is not preferable. But it has by far the better χ^2-value than the a $A^{-1/3}+b$ type or the a $A^{-2/3}+b$ type dependence. From the best of our knowledge we conclude that the mean square radius of the effective two-body interaction is a $A^{2/3}+b$ type. In that sense the formula of $\langle r^2\rangle_{\text{int}}$ is an experimental one.

7. Comparison between experimentally obtained $\langle r^2\rangle_{\text{pot}}$-value and microscopic calculations

In the preceding section it was pointed out that there is a difference

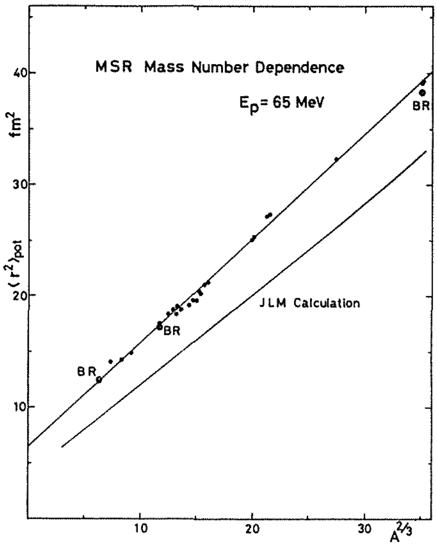

Fig. 12. Mean square radii deduced from the best fit optical potential are compared with the recent microscopic optical potential calcutations. The ⦿ sympols denote Brieva-Rook values interpolated to E_p=65 MeV. The solid line marked JLM is obtained from the optical potential with the microscopically derived parameters of Jeukenne, Lejeune and Mahaux.

between $\langle r^2\rangle_{\text{matt}}$ and $\langle r^2\rangle_{\text{pot}}$ in the target mass number dependence. This difference was reduced to the mass number dependence of the effective two-body interaction. In Fig. 12 the calculated values based on the recent microscopic theories are shown with the experimental $\langle r^2\rangle_{\text{pot}}$-values. The line labeled JLM is the calculation using the JLM model. A detailed explanation of the JLM calculation will be given in Sec. 9. Brieva and Rook calculated the $\langle r^2\rangle_{\text{pot}}$-values of ^{16}O, ^{40}Ca and ^{208}Pb for several incident energies and their $\langle r^2\rangle_{\text{pot}}$-values varied smoothly with energy. The points labeled BR show the interpolation to 65 MeV proton energy of the BR calculations. The BR calculation reproduces remarkably our experimental values shown as the line labeled Kyoto data, although the BR value for ^{208}Pb is a little smaller than the observed value. Calculations in the JLM model differ greatly from the experimental values (by 2~5 fm^2) and cannot reproduce the slope of the mass number dependence. Lejeune and Hodgson[47] pointed out that JLM calculation does not explain the $\langle r^2\rangle_{\text{pot}}$-values and angular distributions, and must be modified by introducing a phenomenological range parameter. Such a phenomenological parameter, however, will mask the validity of the theory to study the dynamics of the reaction. The main origin of the discrepancy may be in the LDA approximation used to transform the optical potential in nuclear matter to the optical potential in a finite nucleus. These two types of microscopic calculations suggest that the density dependence of the effective two-body interaction at the nuclear surface plays an essential role in explaining the A-dependence of the $\langle r^2\rangle_{\text{int}}$-value. It was already pointed out in nuclear matter theory that there is a density dependence[47] in the nuclear matter effective interaction. As the density decreases, the effective two-body interaction increases due to the Pauli principle, and the depth of the optical potential well increases. But the A-dependence of $\langle r^2\rangle_{\text{int}}$ is not explained by the density dependent JLM interaction using the

LDA alone, because the slope of the JLM calculation on the target mass number A is different from the experimentally observed one. (see Fig. 12) On the other hand, when obtaining the t-matrix of the r-representation by BR's calculation, the momentum sum up to the Fermi momentum gives another contribution to the density dependence[48] of the interaction, in addition to the depndence coming explicitly from the Pauli principle. From our present knowledge of the BR calculation, we cannot discern the primary origin of the A-dependence of $\langle r^2\rangle_{\mathrm{int}}$.

8. Root mean square radius of the point nucleon distribution of the target nucleus

Applying the results obtained in the preceding section, we can extract the root mean square radius of the point nucleon distribution of the target nucleus, as follows

$$\langle r^2\rangle^{1/2}_{\mathrm{matt}} = (\langle r^2\rangle_{\mathrm{pot}} - \langle r^2\rangle_{\mathrm{int}})^{1/2}.$$

where

$$\langle r^2\rangle_{\mathrm{int}} = 4.24 \pm 0.24 + (0.132 \pm 0.013) A^{2/3}\ \mathrm{fm}^2$$

The calculated $\langle r^2\rangle^{1/2}_{\mathrm{matt}}$-values from our elastic scattering data are listed in Table 3, together with the 800 MeV polarized proton elastic scattering results from LAMPF. The LAMPF $\langle r^2\rangle^{1/2}_{\mathrm{matt}}$-values were calculated from the proton MSR values $\langle r^2\rangle_p$ and the neutron MSR values $\langle r^2\rangle_n$ of their data,[31),33)] using the relation

$$\langle r^2\rangle^{1/2}_{\mathrm{matt}} = \left(\frac{N}{A}\langle r^2\rangle_n + \frac{Z}{A}\langle r^2\rangle_p\right)^{1/2}$$

Although the LAMPF $\langle r^2\rangle_n$ and $\langle r^2\rangle_p$ values are model dependent, they are thought to be relatively free from the dynamical effects on the nucleon-nucleon interaction in the nucleus. We notice in Table 3 that our values agree remarkably well with the LAMPF results. This indicates the validity of our procedure for extracting the $\langle r^2\rangle_{\mathrm{int}}$-value and the mass number dependence of the effective interaction range. We have thus obtained a new method to extract $\langle r^2\rangle^{1/2}_{\mathrm{matt}}$ value from polarized proton elastic scattering.

9. Volume Integral of the real central part of the optical potential

In the folding model the volume integral J_R of the real central part of the optical potential is calculated as

$$\begin{aligned} J_R &= \int V(\boldsymbol{r}_0)\, \mathrm{d}\boldsymbol{r}_0{}^3 \\ &= \int \mathrm{d}\boldsymbol{r}_0{}^3 \int \mathrm{d}\boldsymbol{r}^3 \rho(r) V_{\mathrm{int}}(|\boldsymbol{r}-\boldsymbol{r}_0|) \end{aligned}$$

Table 3. Volume integral per nucleon and mean square radius of the real central part of the optical potential are listed together with error bars. The effective interaction range and the nuclear matter radius are listed and compared with LAMPF-values. LAMPF-values are calculated by $\langle r^2\rangle^{1/2}_{\mathrm{matter}}=\left(\frac{N}{A}\langle r^2\rangle_n+\frac{Z}{A}\langle r^2\rangle_p\right)^{1/2}$.

Nuclei	$J_R A$ (MeV fm^3)	$\langle r^2\rangle_{\mathrm{pot.}}$ (fm^2)	$\langle r^2\rangle_{\mathrm{int.}}$ (fm^2)	$\langle r^2\rangle^{1/1}_{\mathrm{matter}}$ (fm) Kyoto	LASL
^{16}O	$346.8^{+14.2}_{-9.4}$	$12.35^{+0.06}_{-0.26}$	5.08	2.70	—
^{20}Ne	$349.5^{+9.64}_{-11.3}$	$14.14^{+0.02}_{-0.06}$	5.21	2.99	—
^{24}Mg	$303.0^{+15.3}_{-14.5}$	$14.32^{+0.07}_{-0.23}$	5.34	3.00	—
^{28}Si	$325.3^{+7.8}_{-14.0}$	$14.92^{+0.06}_{-0.07}$	5.46	3.08	—
^{40}Ar	$330.4^{+7.4}_{-11.5}$	$17.54^{+0.05}_{-0.28}$	5.78	3.43	—
^{40}Ca	$333.6^{+5.2}_{-8.6}$	$17.58^{+0.01}_{-0.18}$	5.78	3.43	3.39
^{44}Ca	$318.8^{+5.7}_{-8.5}$	$18.39^{+0.03}_{-0.18}$	5.89	3.54	3.48
^{48}Ca	$315.0^{+6.9}_{-7.5}$	$18.39^{+0.07}_{-0.09}$	5.98	3.52	3.47
^{46}Ti	$317.24^{+4.6}_{-5.9}$	$18.79^{+0.16}_{-0.10}$	5.93	3.59	—
^{48}Ti	$313.1^{+4.9}_{-4.0}$	$19.08^{+0.06}_{-0.10}$	5.98	3.62	—
^{50}Ti	$309.7^{+5.3}_{-3.5}$	$18.82^{+0.08}_{-0.03}$	6.03	3.58	—
^{54}Fe	$303.1^{+5.9}_{-5.1}$	$19.18^{+0.14}_{-0.24}$	6.13	3.61	3.57
^{56}Fe	$307.1^{+2.8}_{-3.2}$	$19.69^{+0.07}_{-0.16}$	6.17	3.68	—
^{59}Co	$307.8^{+4.6}_{-4.0}$	$20.47^{+0.09}_{-0.09}$	6.24	3.77	—
^{58}Ni	$300.2^{+2.6}_{-2.0}$	$19.63^{+0.06}_{-0.20}$	6.22	3.66	3.67 or 3.70
^{60}Ni	$306.8^{+2.1}_{-3.4}$	$20.25^{+0.07}_{-0.12}$	6.26	3.74	—
^{62}Ni	$309.4^{+5.1}_{-5.0}$	$21.07^{+0.21}_{-0.19}$	6.31	3.84	—
^{64}Ni	$315.1^{+3.3}_{-3.2}$	$21.27^{+0.05}_{-0.12}$	6.35	3.86	3.86
^{89}Y	$323.4^{+2.7}_{-2.4}$	$25.09^{+0.1}_{-0.35}$	6.87	4.27	—
^{90}Zr	$318.9^{+1.3}_{-4.4}$	$25.35^{+0.19}_{-0.41}$	6.89	4.30	4.25
^{98}Mo	$321.0^{+2.7}_{-5.8}$	$27.20^{+0.30}_{-0.13}$	7.05	4.49	—
^{100}Mo	$326.0^{+3.4}_{-1.0}$	$27.38^{+0.16}_{-0.31}$	7.08	4.51	—
^{144}Sm	$317.4^{+3.4}_{-2.2}$	$32.18^{+0.23}_{-0.39}$	7.87	4.93	—
^{208}Pb	$330.7^{+2.3}_{-7.0}$	$39.18^{+0.64}_{-0.64}$	8.87	5.51	5.55
^{209}Bi	$319.7^{+3.3}_{-3.6}$	$39.36^{+0.46}_{-0.71}$	8.89	5.52	—

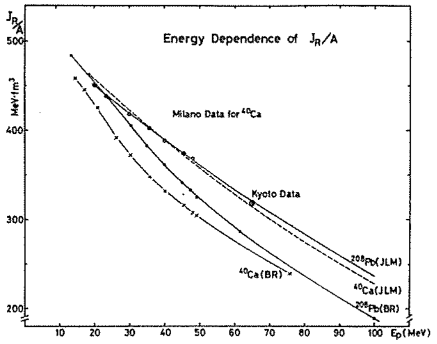

Fig. 13. Volume integral values per nucleon of the optical potentials are plotted as a function of incident proton energy. Open circles are Milan data for ^{40}Ca and double circle is a mean value over 25 targets at $E_p=65$ MeV. The solid dots the and crosses are calculated microscopically by Brieva and Rook, connected by curves meant to guide the eyes. The solid line and the broken line labeled JLM are calculated values using procedure of Jeukenne, Lejeune and Mahaux.

$$= A \int V_{\text{int}}(a)\, \mathrm{d}\boldsymbol{a}^3$$

The volume integral value J_R is proportional to the target mass number if the effective two-body interaction potential between the projectile and the target nucleon is independent of density and energy. A linear fit to J_R-values confirms the approximate validity of the above assumption at 65 MeV, and the volume integral is expressed as

$$J_R = (318 \pm 3)\, A \quad \text{MeV fm}^3$$

In order to show how the recent microscopic calculation explain the empirical volume integral values, J_R/A-values are plotted as a function of incident proton energy in Fig. 13. The double circle point at 65 MeV is the average value of the Kyoto data. The open circles show the recent measurement for ^{40}Ca by the Milan group.[13),14)] We notice that the Kyoto data lie on a smooth extrapolation of lower energy Milan data. The solid and dashed curves labeled JIM indicate the volume integral of the microscopic optical potential calculated in the JLM model. According to the parameter table of the JLM calculation[4)] the optical potential in infinite nuclear matter is obtained as a function of the matter density and the incident projectile energy. As for the point nucleon density distribution for the JLM calculation, we used Negele's density distribution obtained from the fitting to the electron scattering data as in JLM's work. The solid curve shows the calculation for ^{208}Pb and the dashed curve shows the ^{40}Ca case. The results of Brieva-Rook calculation are indicated by the points marked with a cross in the figure for ^{40}Ca and ^{208}Pb nuclei; the curves connecting these points are only meant to guide the eye. As is evident from the figure, the J_R/A value and its bombarding energy dependence are reproduced remarkably well by the JLM calculation. The local density approximation used in the JLM model seems to be effective for the J_R calculation. The energy dependence and the density dependence of the nuclear matter t-matrix are directly reflected in the JLM nuclear optical potential. On the other hand Brieva and Rook transformed the nuclear matter t-matrix in momentum-representation to the t-matrix in the r-representation using a suitable approximation. They then calculated the optical potentials for finite nuclei by applying the folding approximation. The calculation of BR explains the empirical results at 30 MeV, but deviates from the observed values at higher energies. The origin of the descrepancy between the BR's calculation and the experimental data seems to be due to the approximation in their transformation to the r-representation.

In Fig. 14 our J_R/A values listed in Table 3 are plotted as a function of the target mass number. Error bars in the figure were defined similar as the error bars of $\langle r^2\rangle_{\mathrm{pot}}$-values in Sec. 5 but in this case were deduced from the potential parameters at $\chi^2_{\min}(V_r)=1.25\,\chi^2_0$ (best fit), so the error bars have no statistical meaning. Although observed J_R/A values scatter considerably, we notice the following global behavior around the average value of $J_R/A=318$ MeV. As the mass number A increases, the J_R/A value decreases

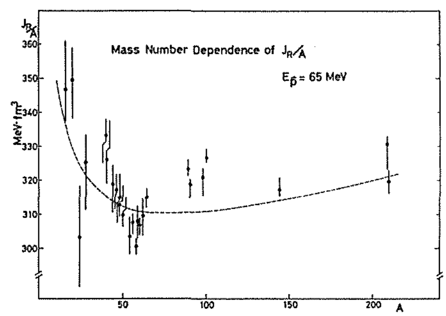

Fig. 14. Volume integral values per nucleon of the real central part of the optical potentials are plotted as a function of the target mass number A. The difinition of the error bars is given in the text. The dashed curve is the JLM model calculation for E_p=65 MeV.

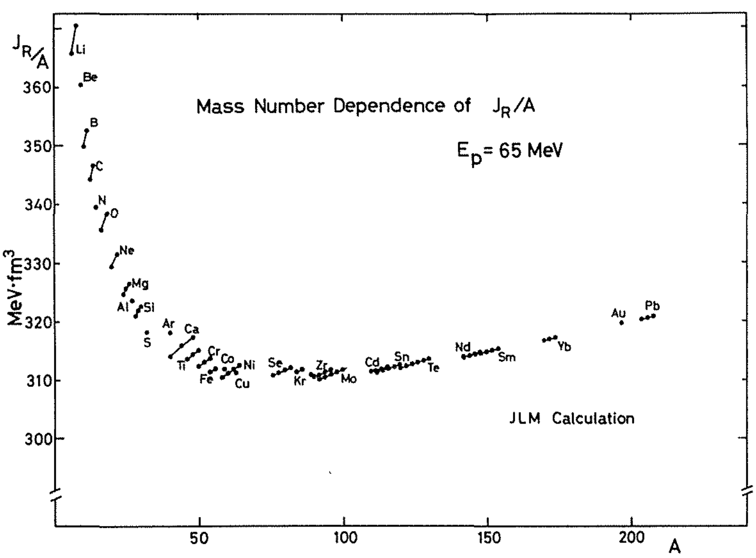

Fig. 15. Volume integral values per nucleon of the real central part of the optical potentials are plotted for each isotope, using Juekenne, Lejeune and Mahaux's model.

rapidly to the minimum in the Fe-Ni region and then increases gradually toward the Pb-Bi region. This global trend is remarkably reproduced by the JLM model calculation shown by the dashed curve in Fig. 14. According to the JLM model, the effective interaction is density dependent. In the lower density region, the effective interaction is stronger[3),4)] due to the smaller Pauli blocking effect. The surface-to-volume ratio is large in light nuclei. As the target mass number increases, the surface-to-volume ratio decreases as $A^{-1/3}$ and the J_R/A-value decreases rapidly. The second gradual increase is explained in the JLM model by the isospin dependent interaction and by the velocity dependence of the effective interaction. (As the mass number increasses, the velocity of the projectile inside the nucleus decreases due to the repulsive Coulomb potential.) This global trend in Fig. 14 is similar to the binding energy per nucleon curve, if we remind that the Coulomb potential is included in the binding energy calculation and the velocity dependent effect is included in the J_R/A calculation. The rapid change in J_R/A-values for lighter nuclei evident in Fig. 14 is possibly evidence of the density dependence of the effective interaction.

10. Anomalous isotope dependence of the real central part of the optical potential in the *f-p* shell region nuclei

C. M. Perey and F. C. Perey analyzed the elastic scattering of 11 MeV polarized protons on 20 target isotopes from ^{48}Ti to ^{76}Ge. For the depth of the real central part of the optical potential they obtained an anomalous linear relation of $V_R = V_0 + \alpha A$ without the isospin dependence. At 65 MeV incident proton energy a similar anomaly was reported in our previous work.[20)] Our previous conclusion was that there must be a linear mass number dependence of $V_{\tau T} = -1.8 + 0.72(A-40)$ in the real isospin dependent part of the optical potential. In Fig. 16 the volume integral values per nucleon are plotted versus $(N-Z)/A$. The slope of the line connecting the same isotopes changes from negative to positive as the mass number of the isotope increases from ^{40}Ca to ^{64}Ni. In the case of the ordinary isospin dependence

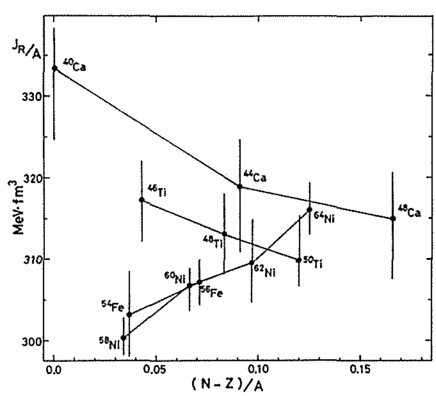

Fig. 16. Observed J_A/A-values are plotted versus $(N-Z)/A$ for *f-p* shell nuclei. The definition of the uncertainties is the same as in Fig. 14.

the slope must be constant. The observed behavior in Fig. 16 is anomalous in this respect. As shown in Fig. 15, the global JLM microscopic model predicts always the positive slope in this mass number region. So it cannot explain the anomalous isotope dependence.

Using our mean square matter radius data in Sec. 5 and the diffuseness value obtained by fitting to the electron scattering data we now have a new density distributions for each target nuclei. The density distribution is assumed to be the Fermi type.

$$\rho(r) = \frac{\rho_0}{1+\exp((r-R_m)/a_m)}$$

where the R_m value is calculated from the formula;

$$\langle r^2\rangle_{\text{nucleon}} + \langle r^2\rangle_{\text{matt}} = \frac{3}{5}R_m{}^2 + \frac{7}{5}\pi^2 a_m{}^2$$

and $a_m = 0.470$ is obtained in Sec. 5 by fitting to the electron scattering data. $\langle r^2\rangle_{\text{nucleon}}$ is the mean square radius of a nucleon and is estimated to be as same as $\langle r^2\rangle_{\text{proton}}$ (0.64 fm^2).

Using this density distribution and the JLM model, the volume integrals of the real central part of the optical potential are calculated for each target nuclei. The calculated J_R/A-values are shown in Fig. 17. The main part of the anomalous isotope effect is reproduced by the JLM model calculations using our new matter distribution data. The origin of the anomalous isotope effect consist of two parts, the density dependence of the effective interaction and the shell closure effect. For nuclei with $N=28$ the size of the nucleus is contracted comparative to their neighbouring nuclei. Since the matter density for the $N=28$ nuclei increases, the strength of the effective interaction is reduced according to its density dependence. Thus for nuclei $A \leq 53$ the J_A/A value takes the negative slope versus the mass number. But in the figure we notice differences between calculation and experimental data, which will be explained only by the nuclear structure dependent effective interaction.

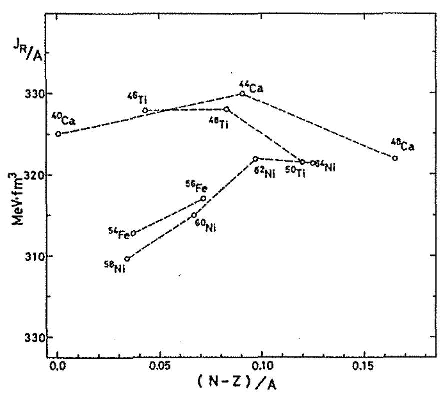

Fig. 17. Calculated J_R/A-values are plotted versus $(N-Z)/A$ for f-p shell nuclei.

11. Conclusions

We have systematically measured polarized proton elastic scattering from 25 targets at 65 MeV. An optical potential analysis gave good fits to both cross section data and analyzing power data. By plotting the mean square radius of the real central part of the optical potential versus $A^{2/3}$, we have obtained the global systematics of the MSR of the potential as $\langle r^2\rangle_{\mathrm{pot}} = (6.42 \pm 0.21) + (0.937 \pm 0.012)\, A^{2/3}$ fm^2. Using the simple folding model and by comparing with the charge distribution obtained by electron scattering, we found that the effective interaction range has a mass number dependence of the form

$$\langle r^2\rangle_{\mathrm{int}} = (4.24 \pm 0.24) + (0.132 \pm 0.013)\, A^{2/3}\ \mathrm{fm}^2.$$

Assuming this mass number dependence of the effective interaction range, we have obtained root mean square radii of the point nucleon distribution, which are in accord with the high energy LAMPF data and reflect the shell effect and the individual characteristics of the target nuclei. This mass number dependence of $\langle r^2\rangle_{\mathrm{int}}$ was shown to be different for different projectiles such as d, ^{3}He or α.

For nuclei of $A<58$, the J_R/A value decreases as the mass number of the target increases. This rapid decrease was interpreted as evidence of the density dependence of the effective interaction. The JLM model explains both energy and A dependence of the J_R/A but cannot explain the value of $\langle r^2\rangle_{\mathrm{pot}}$, and its A-dependence.

On the other hand the BR calculation reproduces our $\langle r^2\rangle_{\mathrm{pot}}$-values but could not predict the J_R/A-values, especially the energy dependence of J_R/A. At present, each of the two global theories could explain the experimental results only partially, but is found to be an effective guide in clarifying nuclear many body dynamics. The anomalous isotope dependence of J_R/A is explained qualitatively by the JLM density dependent interaction and the matter radius obtained from our experiment.

ACKNOWLEDGEMENTS

The experimental group consisted of Prof. S. Kobayashi, Mr. M. Nakamura, Dr. K. Hatanaka, Dr. Goto, Mr. T. Noro, Mr. F. Ohtani, Mr. H. Sakamoto and Mr. H. Ogawa, all of whom devoted a large amount of time and effort throughout the experiment. Their execellent collaborations at the every stage of the experiment from target preparation to data analysis are greatly appreciated. The author is particularly indebted to Prof. S. Kobayashi for his efficient guidances and suggestions not only during the experiment but also in the stage of the analysis and the appreciation of the deduced quantities. The success of this long run experiment is also attributed to the cyclotron crew under Prof. M. Kondo of Research Center for Nuclear Physics, Osaka

University and the polarized ion source team under Prof. K. Nishimura of Kyoto University. Their wonderful operation of the cyclotron and the polarized ion source are greatly appreciated. Sincere thanks are also expressed to Prof. H. Ogata, Prof. K. Hosono and Dr. N. Matsuoka of RCNP, Osaka University for their hospitalities during the experiment. The author owes thanks to Prof. S. Nagata of Miyazaki University for fruitful discussions on the microscopic optical potential. He is also grateful to Mrs. E. Takahashi and other secretaries for their patience in typing the manuscript.

Appeneix: Table of Differential Cross Section and Analyzing Power Values

Table 4. Experimental data.

^{16}O

Angle	Cross Section (mb/sr)	Analyzing power
18.59	589.4 ±1.0	0.0563±0.0030
21.23	405.60 ±0.89	0.0459±0.0036
23.88	261.47 ±0.75	0.0407±0.0049
26.53	156.66 ±0.33	0.0361±0.0035
29.17	86.00 ±0.35	0.0433±0.0066
31.81	45.07 ±0.19	0.0950±0.0070
34.44	22.88 ±0.14	0.266 ±0.0106
37.07	13.45 ±0.11	0.560 ±0.015
39.70	9.818 ±0.099	0.864 ±0.018
42.32	8.876 ±0.066	0.972 ±0.016
44.94	8.403 ±0.068	0.948 ±0.020
47.55	7.832 ±0.065	0.875 ±0.016
50.16	7.359 ±0.070	0.801 ±0.017
52.77	5.492 ±0.040	0.780 ±0.014
55.37	4.287 ±0.048	0.704 ±0.019
57.96	2.946 ±0.044	0.654 ±0.024
60.55	2.135 ±0.027	0.618 ±0.021
63.13	1.492 ±0.017	0.565 ±0.020
65.70	1.079 ±0.011	0.478 ±0.020
68.27	0.809 ±0.017	0.513 ±0.035
70.84	0.691 ±0.015	0.479 ±0.034
73.39	0.628 ±0.014	0.483 ±0.037
75.95	0.540 ±0.012	0.436 ±0.036
78.49	0.490 ±0.012	0.494 ±0.039
83.56	0.344 ±0.011	0.549 ±0.057
93.61	0.0982 ±0.0033	0.659 ±0.059
108.49	0.00886±0.00079	0.37 ±0.16

^{20}Ne

Angle	Cross Section (mb/sr)	Analysing power
18.37	663.56 ±0.82	0.0410±0.0023
23.61	244.26 ±0.40	0.0096±0.0029
26.22	126.96 ±0.30	0.0066±0.0043
28.84	60.81 ±0.22	0.0501±0.0063
31.45	27.64 ±0.16	0.220 ±0.010
34.05	15.37 ±0.12	0.550 ±0.015
36.66	11.75 ±0.11	0.850 ±0.017
39.26	11.54 ±0.11	0.918 ±0.018
41.86	10.97 ±0.11	0.844 ±0.020
44.45	10.139 ±0.097	0.781 ±0.018
47.04	8.537 ±0.071	0.698 ±0.015
49.63	6.374 ±0.058	0.667 ±0.017
52.21	4.314 ±0.051	0.618 ±0.022
54.79	2.309 ±0.029	0.579 ±0.022
57.37	1.825 ±0.025	0.608 ±0.023
59.94	1.203 ±0.023	0.584 ±0.027
62.50	0.855 ±0.014	0.691 ±0.030
65.06	0.678 ±0.015	0.716 ±0.036
67.62	0.509 ±0.013	0.789 ±0.040
70.17	0.474 ±0.012	0.819 ±0.044
72.72	0.388 ±0.011	0.889 ±0.045
75.26	0.341 ±0.011	0.861 ±0.052
77.79	0.2671±0.0078	0.909 ±0.046
82.85	0.1408±0.0056	0.984 ±0.063
87.88	0.0559±0.0037	0.956 ±0.108
92.89	0.0304±0.0019	0.93 ±0.12

^{24}Mg

Angle	Cross Section (mb/sr)	Analysing power
14.10	1421.6 ±1.2	0.0745±0.0021
15.66	1183.7 ±1.4	0.0605±0.0027
20.88	481.17 ±0.96	0.0126±0.0038
23.48	265.63 ±0.36	0.0012±0.0025
26.09	128.19 ±0.35	−0.0022±0.0053
28.68	55.79 ±0.16	0.0789±0.0059
31.28	25.19 ±0.11	0.370 ±0.010
33.88	16.40 ±0.089	0.814 ±0.015
36.47	15.883 ±0.087	0.924 ±0.017
39.06	17.015 ±0.090	0.808 ±0.015
41.65	16.516 ±0.089	0.711 ±0.014
41.65	16.630 ±0.063	0.727 ±0.012
44.23	14.489 ±0.084	0.617 ±0.014
46.81	11.542 ±0.075	0.577 ±0.014
48.88	8.877 ±0.054	0.528 ±0.013
51.96	5.530 ±0.037	0.509 ±0.014
59.66	1.815 ±0.017	0.671 ±0.019
62.22	1.432 ±0.015	0.759 ±0.021
67.32	1.033 ±0.011	0.904 ±0.021
72.41	0.6922 ±0.0088	0.978 ±0.026
77.48	0.3840 ±0.0047	0.979 ±0.023
82.52	0.1787 ±0.0023	0.945 ±0.023
87.55	0.0872 ±0.0018	0.676 ±0.037
92.56	0.0639 ±0.0011	0.360 ±0.032
100.04	0.0513 ±0.0012	0.209 ±0.045
117.32	0.00912±0.00060	0.47 ±0.12
124.66	0.00247±0.00032	0.58 ±0.23

^{28}Si

Angle	Cross Section (mb/sr)	Analyzing Power
14.53	1493 ±30	0.0598±0.0030
16.61	1089 ±22	0.0367±0.0030
18.68	750 ±15	0.0171±0.0040
20.75	479.4 ± 9.7	0.0028±0.0050
22.82	284.5 ± 5.8	0.0133±0.0060
24.90	153.3 ± 3.1	0.0193±0.0060
26.96	76.3 ± 1.6	0.0314±0.0080
29.03	39.31 ± 0.86	0.254 ±0.012
31.10	24.33 ± 0.52	0.648 ±0.012
33.68	21.14 ± 0.46	0.918 ±0.014
36.26	23.98 ± 0.52	0.853 ±0.013
38.84	24.91 ± 0.54	0.735 ±0.012
41.41	22.78 ± 0.49	0.631 ±0.012
43.99	18.58 ± 0.41	0.557 ±0.013
46.56	13.62 ± 0.30	0.520 ±0.014
49.12	9.08 ± 0.20	0.482 ±0.013
51.68	6.00 ± 0.15	0.455 ±0.019
54.24	3.889 ± 0.087	0.569 ±0.014
56.80	2.766 ± 0.062	0.668 ±0.014
59.35	2.188 ± 0.049	0.808 ±0.014
61.90	1.920 ± 0.042	0.900 ±0.014
64.45	1.689 ± 0.038	0.947 ±0.014
66.99	1.386 ± 0.030	0.983 ±0.014
69.41	1.1422± 0.0075	0.997 ±0.013
74.47	0.6346± 0.0043	0.992 ±0.013
79.52	0.2872± 0.0026	0.861 ±0.013
82.03	0.2019± 0.0019	0.674 ±0.013
84.55	0.1623± 0.0018	0.492 ±0.014
87.06	0.1389± 0.0016	0.287 ±0.013
89.56	0.1312± 0.0016	0.199 ±0.013
94.56	0.1147± 0.0015	0.181 ±0.011

^{40}Ar

Angle	Cross Section (mb/sr)	Analyzing Power
17.93	906.0 ±3.7	−0.0508±0.0037
20.49	411.6 ±1.3	−0.0916±0.0060
23.05	154.41 ±0.86	−0.131 ±0.010
25.61	52.23 ±0.52	0.114 ±0.019
28.18	37.64 ±0.34	0.729 ±0.019
30.72	46.90 ±0.59	0.772 ±0.015
33.28	59.52 ±0.47	0.627 ±0.017
35.83	56.16 ±0.39	0.522 ±0.014
38.38	46.17 ±0.31	0.437 ±0.013
40.93	30.04 ±0.30	0.376 ±0.019
43.48	18.56 ±0.13	0.320 ±0.013
46.02	9.365±0.143	0.402 ±0.027
48.56	5.692±0.076	0.568 ±0.024
51.11	4.342±0.055	0.873 ±0.022
53.65	4.022±0.066	0.989 ±0.027
56.18	3.887±0.047	0.989 ±0.021
58.72	3.693±0.066	0.906 ±0.029
61.25	2.972±0.042	0.860 ±0.024
63.78	2.084±0.051	0.766 ±0.039
66.31	1.275±0.035	0.774 ±0.039
68.83	0.935±0.035	0.679 ±0.060
71.36	0.631±0.020	0.667 ±0.062
73.88	0.488±0.026	0.561 ±0.087
76.40	0.446±0.017	0.675 ±0.068

^{40}Ca

Angle	Cross Section (mb/sr)	Analyzing Power
15.17	1403.7 ±2.4	0.0280±0.0025
16.20	1146.7 ±2.2	−0.0061±0.0027
17.22	885.9 ±1.9	−0.0168±0.0031
18.24	682.3 ±1.7	−0.0670±0.0036
19.27	511.3 ±1.5	−0.0777±0.0042
20.29	358.6 ±1.2	−0.1178±0.0049
21.31	261.5 ±1.1	−0.1350±0.0061
22.34	175.91 ±0.70	−0.1653±0.0054
23.36	115.59 ±0.61	−0.1450±0.0068
25.41	48.18 ±0.45	0.0050±0.0082
26.43	33.74 ±0.38	0.338 ±0.016
27.45	30.66 ±0.25	0.573 ±0.012
28.47	28.14 ±0.34	0.821 ±0.019
29.50	31.56 ±0.37	0.876 ±0.021
30.52	36.37 ±0.39	0.835 ±0.019
33.07	43.76 ±0.20	0.6807±0.0096
35.88	44.03 ±2.20	0.5285±0.0063
38.17	37.32 ±0.18	0.4529±0.0083
40.99	25.81 ±1.29	0.3808±0.0047
43.27	16.15 ±0.12	0.359 ±0.011
46.09	9.133±0.457	0.3738±0.0058
51.18	3.956±0.198	0.820 ±0.010
53.44	3.392±0.045	0.959 ±0.018
56.26	3.402±0.170	0.993 ±0.012
58.51	2.832±0.032	0.963 ±0.016
61.33	2.470±0.124	0.903 ±0.012
66.40	1.226±0.061	0.778 ±0.011
76.49	0.508±0.025	0.723±0.016
81.52	0.448±0.022	0.750±0.038
86.53	0.293±0.015	0.895±0.044

^{44}Ca

Angle	Cross Section (mb/sr)	Analyzing Power
15.16	1581.3 ±2.0	0.0002±0.0020
16.18	1227.8 ±3.9	−0.0234±0.0050
17.72	827.7 ±1.4	−0.0575±0.0030
19.25	505.5 ±2.5	−0.0937±0.0070
20.28	355.45 ±0.93	−0.1262±0.0041
21.30	227.13 ±1.02	−0.1487±0.0060
22.32	149.49 ±0.47	−0.1593±0.0051
23.34	88.16 ±0.57	−0.1398±0.0090
24.37	56.63 ±0.29	0.0076±0.0079
25.39	35.75 ±0.36	0.334 ±0.013
26.41	29.51 ±0.27	0.670 ±0.013
27.43	33.60 ±0.25	0.828 ±0.014
28.45	38.26 ±0.24	0.843 ±0.012
29.48	44.95 ±0.33	0.771 ±0.014
30.50	50.95 ±0.27	0.743 ±0.011
33.05	59.90 ±0.22	0.5586±0.0080
35.60	54.67 ±0.29	0.4594±0.0095
38.15	41.60 ±0.13	0.3760±0.0065
40.70	26.81 ±0.20	0.318 ±0.011
43.24	14.783±0.076	0.3098±0.0082
45.79	7.757±0.078	0.405 ±0.014
48.33	4.874±0.039	0.689 ±0.013
50.87	4.295±0.041	0.946 ±0.015
53.41	4.211±0.036	0.996 ±0.015
55.94	4.063±0.036	0.944 ±0.015
58.48	3.378±0.033	0.860 ±0.015
61.01	2.649±0.023	0.822 ±0.014
66.07	1.154±0.014	0.697 ±0.017
71.11	0.604±0.010	0.688 ±0.021

^{48}Ca

Angle	Cross Section (mb/sr)	Analyzing Power
24.49	42.30 ±0.84	0.160 ±0.020
25.51	36.12 ±0.78	0.544 ±0.019
26.53	37.97 ±0.80	0.775 ±0.020
27.55	44.19 ±0.86	0.831 ±0.016
28.57	54.69 ±0.96	0.760 ±0.018
29.58	64.62 ±1.04	0.678 ±0.014
30.60	71.68 ±1.10	0.6026±0.0096
33.14	77.90 ±0.74	0.473 ±0.011
35.69	66.63 ±0.49	0.3875±0.0080
38.24	46.13 ±0.40	0.2990±0.0092
40.77	27.46 ±0.31	0.247 ±0.012
43.31	13.81 ±0.16	0.300 ±0.012
45.85	7.650±0.134	0.499 ±0.018
48.39	5.952±0.103	0.885 ±0.016
50.92	6.230±0.086	0.988 ±0.013
53.46	6.361±0.095	0.948 ±0.014
55.99	5.915±0.073	0.871 ±0.012
58.52	4.696±0.075	0.801 ±0.015
61.04	3.220±0.054	0.711 ±0.015
63.57	2.190±0.051	0.689 ±0.022
66.09	1.299±0.028	0.575 ±0.020
68.61	0.958±0.026	0.635 ±0.026
71.13	0.826±0.022	0.761 ±0.023

^{46}Ti

Angle	Cross Section (mb/sr)	Analyzing Power
15.35	1793.1 ±8.3	−0.0095±0.0063
16.37	1396.4 ±5.2	−0.0338±0.0050
17.39	1067.7 ±6.4	−0.0426±0.0080
18.42	771.4 ±3.9	−0.0771±0.0066
19.44	535.1 ±3.2	−0.1125±0.0084
20.46	373.6 ±2.2	−0.1440±0.0080
21.48	242.1 ±2.2	−0.165 ±0.012
22.50	147.0 ±1.1	−0.176 ±0.010
23.52	88.98 ±0.83	−0.116 ±0.013
24.55	54.59 ±0.51	0.0025±0.0127
25.57	38.30 ±0.43	0.381 ±0.015
26.59	35.41 ±0.52	0.704 ±0.018
27.61	37.93 ±0.43	0.825 ±0.016
28.63	45.51 ±0.42	0.826 ±0.014
29.65	52.74 ±0.50	0.762 ±0.015
30.67	60.89 ±0.49	0.664 ±0.012
33.22	67.64 ±0.52	0.515 ±0.011
35.77	59.33 ±0.49	0.419 ±0.012
38.32	43.11 ±0.42	0.342 ±0.013
40.86	26.63 ±0.23	0.273 ±0.012
43.41	14.05 ±0.17	0.270 ±0.016
45.95	8.050±0.104	0.422 ±0.016
48.49	5.195±0.084	0.768 ±0.020
51.03	4.827±0.070	1.001 ±0.017
56.10	4.450±0.060	0.994 ±0.018
61.16	2.674±0.038	0.779 ±0.018
63.69	1.777±0.043	0.683 ±0.029
66.22	1.147±0.024	0.675 ±0.026
68.74	0.860±0.021	0.648 ±0.030

^{48}Ti

Angle	Cross Section (mb/sr)	Analyzing Power
15.33	1644.1 ±3.5	−0.0155±0.0028
16.35	1281.1 ±3.1	−0.0360±0.0032
17.38	964.4 ±2.7	−0.0614±0.0037
18.40	694.5 ±2.3	−0.0864±0.0044
19.42	495.7 ±2.4	−0.1012±0.0063
20.44	327.9 ±1.2	−0.1462±0.0051
21.46	212.1 ±1.5	−0.1648±0.0097
22.48	131.35 ±0.77	−0.1693±0.0078
23.50	76.69 ±0.93	−0.087 ±0.016
24.52	49.80 ±0.47	0.096 ±0.012
25.54	36.88 ±0.45	0.448 ±0.016
26.56	35.68 ±0.40	0.753 ±0.015
27.58	40.15 ±0.42	0.822 ±0.015
28.60	48.77 ±0.33	0.781 ±0.012
29.62	57.18 ±0.51	0.707 ±0.013
30.64	63.36 ±0.38	0.631 ±0.010
33.19	68.28 ±0.57	0.494 ±0.012
35.74	60.47 ±0.53	0.391 ±0.012
38.28	42.26 ±0.32	0.301 ±0.010
40.83	24.96 ±0.20	0.242 ±0.011
43.37	13.24 ±0.15	0.279 ±0.015
45.91	7.265±0.070	0.474 ±0.013
48.45	5.361±0.060	0.822 ±0.015
50.99	5.139±0.059	1.006 ±0.015
53.52	5.236±0.060	0.970 ±0.015
56.05	4.724±0.057	0.879 ±0.016
58.58	3.731±0.042	0.810 ±0.015
61.11	2.634±0.035	0.751 ±0.017
63.64	1.764±0.029	0.661 ±0.020
66.16	1.133±0.023	0.618 ±0.025
68.69	0.827±0.020	0.674 ±0.029
71.21	0.696±0.015	0.746 ±0.025

^{50}Ti

Angle	Cross Section (mb/sr)	Analyzing Power
15.32	1670.8 ±6.6	−0.0225±0.0052
16.34	1286.4 ±5.8	−0.0429±0.0059
17.36	956.7 ±3.6	−0.0700±0.0050
18.38	688.4 ±3.0	−0.1019±0.0059
19.40	475.8 ±2.5	−0.1279±0.0071
20.42	312.9 ±2.0	−0.1430±0.0087
21.44	193.6 ±1.6	−0.195 ±0.011
22.46	115.6 ±1.2	−0.172 ±0.014
23.48	69.31 ±0.78	−0.081 ±0.015
24.50	43.96 ±0.62	0.185 ±0.019
25.52	34.68 ±0.43	0.575 ±0.016
26.54	36.43 ±0.44	0.803 ±0.016
27.56	45.52 ±0.49	0.808 ±0.015
28.58	54.92 ±0.54	0.753 ±0.014
29.60	64.23 ±0.58	0.674 ±0.013
30.62	70.84 ±0.61	0.603 ±0.012
33.16	75.68 ±0.65	0.451 ±0.012
35.71	63.72 ±0.27	0.3548±0.0067
38.25	45.46 ±0.41	0.297 ±0.012
40.79	26.00 ±0.17	0.2293±0.0089
43.33	13.59 ±0.16	0.262 ±0.015
45.87	7.610±0.084	0.516 ±0.015
48.41	5.820±0.068	0.899 ±0.015
50.95	6.012±0.058	0.988 ±0.014
53.48	6.077±0.070	0.955 ±0.015
56.01	5.522±0.056	0.861 ±0.014
58.54	4.302±0.049	0.785 ±0.015
61.07	3.020±0.041	0.684 ±0.017
63.59	1.908±0.033	0.660 ±0.021
66.12	1.240±0.027	0.593 ±0.026
68.64	0.990±0.024	0.636 ±0.028
71.16	0.873±0.018	0.753 ±0.024

^{54}Fe

Angle	Cross Section (mb/sr)	Analyzing Power
15.30	2050.3 ±5.7	−0.0162±0.0037
16.32	1522.2 ±4.9	−0.0394±0.0044
17.33	1171.1 ±4.3	−0.0717±0.0050
18.35	809.2 ±3.6	−0.0966±0.0061
19.37	567.0 ±3.0	−0.1528±0.0073
20.39	357.4 ±1.7	−0.1770±0.0067
21.41	223.3 ±1.3	−0.2295±0.0085
22.43	130.10 ±0.83	−0.2206±0.0089
22.94	96.94 ±0.72	−0.184 ±0.010
23.45	73.90 ±0.63	−0.115 ±0.012
24.47	47.17 ±0.50	0.185 ±0.014
25.48	38.70 ±0.45	0.662 ±0.016
25.99	40.85 ±0.47	0.780 ±0.016
26.50	44.04 ±0.48	0.872 ±0.015
27.52	55.26 ±0.47	0.840 ±0.014
28.54	68.96 ±0.47	0.741 ±0.012
29.55	82.19 ±0.51	0.644 ±0.011
30.57	89.93 ±0.54	0.567 ±0.010
33.11	95.52 ±0.40	0.4180±0.0085
35.66	77.07 ±0.36	0.3228±0.0082
38.20	53.84 ±0.30	0.2411±0.0094
40.74	30.58 ±0.23	0.179 ±0.011
43.27	16.09 ±0.17	0.269 ±0.016
45.81	9.759±0.091	0.600 ±0.015
48.34	8.460±0.085	0.892 ±0.017
50.88	8.283±0.068	0.999 ±0.015
53.41	8.097±0.068	0.941 ±0.015
55.94	7.017±0.063	0.835 ±0.015
58.46	5.358±0.055	0.755 ±0.017
60.99	3.674±0.042	0.659 ±0.018
63.51	2.421±0.344	0.587 ±0.022
66.04	1.738±0.024	0.592 ±0.021
68.56	1.431±0.022	0.626 ±0.023
71.07	1.264±0.019	0.734 ±0.021

^{56}Fe

Angle	Cross Section (mb/sr)	Analyzing Power
14.27	2444.8 ±8.0	−0.0161±0.0051
16.30	1417.3 ±8.6	−0.0550±0.0093
18.34	700.1 ±3.0	−0.1253±0.0068
20.38	286.0 ±1.9	−0.243 ±0.011
21.40	165.9 ±1.5	−0.280 ±0.014
22.41	90.24 ±0.88	−0.188 ±0.015
23.43	53.21 ±0.63	0.0028±0.0176
24.45	39.04 ±0.54	0.502 ±0.021
25.47	39.65 ±0.51	0.797 ±0.019
26.48	51.49 ±0.58	0.861 ±0.018
28.52	77.82 ±0.64	0.662 ±0.014
30.55	95.90 ±0.64	0.522 ±0.012
33.09	94.30 ±0.51	0.3896±0.0091
35.63	72.10 ±0.36	0.2965±0.0084
38.17	45.42 ±0.35	0.193 ±0.012
40.71	24.36 ±0.21	0.196 ±0.014
43.24	12.47 ±0.15	0.345 ±0.018
45.78	8.271±0.087	0.738 ±0.017
48.31	7.911±0.093	0.960 ±0.018
50.84	8.217±0.071	0.947 ±0.015
53.37	7.643±0.075	0.886 ±0.017
55.90	6.198±0.062	0.788 ±0.016
58.43	4.376±0.057	0.690 ±0.022
60.95	2.879±0.042	0.601 ±0.022
63.48	1.885±0.029	0.561 ±0.024
66.00	1.333±0.024	0.594 ±0.026
68.52	1.185±0.019	0.716 ±0.023
71.04	1.104±0.018	0.843 ±0.023

^{59}Co

Angle	Cross Section (mb/sr)	Analyzing Power
15.37	1794.9 ±4.9	−0.0523±0.0039
16.39	1311.4 ±4.2	−0.0759±0.0045
17.41	946.6 ±3.5	−0.1165±0.0055
18.43	627.4 ±1.2	−0.1511±0.0031
19.44	407.4 ±1.6	−0.1982±0.0061
20.46	250.60 ±0.74	−0.2451±0.0050
21.48	141.55 ±0.97	−0.266 ±0.010
22.49	80.62 ±0.42	−0.1603±0.0075
23.51	48.59 ±0.57	0.138 ±0.016
24.53	40.75 ±0.52	0.647 ±0.017
25.54	48.32 ±0.40	0.815 ±0.013
26.56	61.72 ±0.64	0.775 ±0.015
27.58	76.99 ±0.51	0.705 ±0.011
28.59	90.88 ±0.77	0.605 ±0.013
29.61	98.70 ±0.57	0.5401±0.0097
30.63	103.07 ±0.83	0.484 ±0.012
31.64	102.44 ±0.58	0.4258±0.0091
33.67	89.67 ±0.54	0.3346±0.0092
35.70	67.30 ±0.39	0.2544±0.0085
38.24	40.18 ±0.30	0.194 ±0.011
40.77	20.76 ±0.21	0.207 ±0.014
43.31	11.26 ±0.13	0.457 ±0.016
45.84	8.736±0.089	0.829 ±0.015
48.37	8.949±0.050	0.956 ±0.012
50.90	8.949±0.079	0.917 ±0.014
53.43	7.961±0.074	0.816 ±0.014
55.96	6.135±0.058	0.752 ±0.014
58.48	4.199±0.048	0.666 ±0.016
61.01	2.659±0.031	0.586 ±0.016
63.53	1.778±0.026	0.607 ±0.019
66.05	1.448±0.020	0.708 ±0.018
71.08	1.240±0.017	0.897 ±0.017
76.11	0.896±0.013	0.968 ±0.018

^{58}Ni

Angle	Cross Section (mb/sr)	Analyzing Power
14.26	2578.8 ±11.1	−0.0199±0.0063
16.29	1503.1 ± 6.1	−0.0705±0.0059
18.33	746.1 ± 3.0	−0.1439±0.0062
20.36	303.7 ± 1.9	−0.2368±0.0095
21.38	174.1 ± 1.2	−0.282 ±0.010
22.40	96.55 ± 0.89	−0.243 ±0.013
23.42	53.62 ± 0.66	−0.0074±0.0175
24.43	38.86 ± 0.49	0.465 ±0.018
24.94	38.71 ± 0.19	0.692 ±0.010
25.45	41.34 ± 0.58	0.842 ±0.020
25.96	46.05 ± 0.61	0.873 ±0.019
26.47	51.12 ± 0.65	0.865 ±0.018
27.48	65.95 ± 0.73	0.768 ±0.017
28.50	82.23 ± 0.82	0.684 ±0.015
30.53	102.34 ± 0.79	0.511 ±0.012
33.07	97.67 ± 0.50	0.3741±0.0089
35.61	75.59 ± 0.44	0.2698±0.0090
38.15	47.63 ± 0.29	0.1999±0.0091
40.68	26.35 ± 0.19	0.176 ±0.010
43.22	13.66 ± 0.12	0.325 ±0.013
45.75	9.169± 0.077	0.735 ±0.014
48.28	8.896± 0.088	0.978 ±0.016
50.82	8.982± 0.076	0.951 ±0.015
53.34	8.513± 0.067	0.869 ±0.014
55.87	6.796± 0.060	0.768 ±0.014
58.40	4.852± 0.041	0.670 ±0.013
60.92	3.188± 0.041	0.562 ±0.018
63.44	2.148± 0.024	0.564 ±0.016
65.96	1.587± 0.020	0.623 ±0.018
68.48	1.404± 0.016	0.734 ±0.016
71.00	1.318± 0.015	0.827 ±0.016

^{60}Ni

Angle	Cross Section (mb/sr)	Analyzing Power
14.25	2776.7 ±28.7	−0.0153±0.0048
16.28	1553.8 ±16.7	−0.0809±0.0068
18.32	725.7 ± 7.8	−0.1531±0.0069
19.34	459.8 ± 5.2	−0.2213±0.0087
20.35	273.7 ± 3.9	−0.285 ±0.016
21.37	152.5 ± 1.9	−0.295 ±0.012
22.38	80.28 ± 1.35	−0.235 ±0.021
23.40	49.38 ± 0.85	0.1447±0.021
24.42	41.59 ± 0.89	0.686 ±0.026
24.93	46.31 ± 0.52	0.819 ±0.012
25.43	51.93 ± 0.76	0.880 ±0.017
26.45	69.70 ± 0.12	0.819 ±0.021
28.48	103.53 ± 1.60	0.602 ±0.018
30.51	120.11 ± 1.32	0.4656±0.0097
33.05	110.36 ± 1.37	0.334 ±0.012
35.59	79.19 ± 0.92	0.2577±0.0098
38.13	46.80 ± 0.60	0.169 ±0.012
40.66	23.70 ± 0.30	0.165 ±0.012
43.20	12.33 ± 0.17	0.409 ±0.015
45.73	9.678± 0.13	0.854 ±0.015
48.26	10.05 ± 0.15	0.982 ±0.017
50.79	10.19 ± 0.14	0.936 ±0.015
53.32	9.07 ± 0.12	0.824 ±0.015
55.84	7.005±0.102	0.728 ±0.016
58.37	4.845±0.073	0.615 ±0.017
60.89	2.985±0.053	0.579 ±0.021
63.41	1.936±0.031	0.547 ±0.019
65.93	1.604±0.028	0.672 ±0.020
68.45	1.495±0.025	0.799 ±0.019
70.97	1.425±0.022	0.877 ±0.018

^{62}Ni

Angle	Cross Section (mb/sr)	Analyzing Power
13.33	3351.6 ±17.8	−0.0094±0.0039
14.34	2585.3 ±14.3	−0.0334±0.0043
16.38	1369.8 ± 8.45	−0.1028±0.0061
18.41	594.7 ± 4.2	−0.2082±0.0082
19.43	365.0 ± 2.6	−0.2624±0.0087
20.44	202.5 ± 1.8	−0.305 ±0.011
21.46	107.7 ± 1.2	−0.303 ±0.015
22.48	57.74 ± 0.68	−0.074 ±0.016
23.49	40.78 ± 0.56	0.510 ±0.019
24.51	45.88 ± 0.60	0.848 ±0.018
25.52	62.84 ± 0.71	0.861 ±0.016
26.54	83.41 ± 1.04	0.736 ±0.018
28.57	116.29 ± 1.27	0.564 ±0.015
30.50	127.56 ± 0.90	0.421 ±0.010
30.60	125.39 ± 1.19	0.424 ±0.013
33.04	108.92 ± 0.80	0.3108±0.095
35.57	73.27 ± 0.61	0.208 ±0.011
38.11	40.07 ± 0.42	0.144 ±0.014
39.12	29.73 ± 0.35	0.145 ±0.017
40.64	19.45 ± 0.28	0.202 ±0.020
43.17	10.85 ± 0.17	0.574 ±0.022
45.70	10.07 ± 0.14	0.939 ±0.020
47.22	10.40 ± 0.13	0.994 ±0.018
48.23	10.89 ± 0.14	0.952 ±0.018
50.76	10.76 ± 0.13	0.889 ±0.018
53.29	8.875± 0.11	0.793 ±0.018
55.82	6.488± 0.093	0.679 ±0.021
58.34	4.055± 0.057	0.591 ±0.020
60.86	2.470± 0.036	0.580 ±0.021
63.38	1.777± 0.030	0.617 ±0.024
65.90	1.515± 0.024	0.729 ±0.022
68.42	1.500± 0.024	0.863 ±0.022

^{65}Ni

Angle	Cross Section (mb/sr)	Analyzing Power
13.32	3256.0 ±11.9	−0.0189±0.0034
14.34	2472.6 ± 9.5	−0.0406±0.0038
16.37	1284.2 ± 5.9	−0.1048±0.0056
18.40	537.6 ± 3.0	−0.2227±0.0080
19.42	312.6 ± 2.5	−0.279 ±0.012
20.43	170.7 ± 1.6	−0.353 ±0.015
21.45	85.54 ± 0.89	−0.295 ±0.015
22.46	49.82 ± 0.58	0.090 ±0.018
23.48	41.23 ± 0.60	0.627 ±0.021
24.49	53.25 ± 0.84	0.832 ±0.024
25.51	74.70 ± 0.72	0.792 ±0.016
26.52	95.05 ± 0.94	0.722 ±0.017
28.55	127.64 ± 1.33	0.514 ±0.016
30.48	132.92 ± 0.70	0.3836±0.0087
30.58	134.37 ± 0.91	0.3866±0.0099
33.02	107.27 ± 0.62	0.2887±0.0085
35.55	68.54 ± 0.47	0.1971±0.0099
38.09	35.89 ± 0.27	0.1277±0.011
39.10	26.63 ± 0.23	0.140 ±0.013
40.62	16.64 ± 0.16	0.247 ±0.014
43.15	10.29 ± 0.12	0.704 ±0.018
44.67	10.11 ± 0.12	0.909 ±0.018
45.68	10.40 ± 0.11	0.985 ±0.017
46.69	10.99 ± 0.11	1.007 ±0.017
48.21	11.74 ± 0.12	0.953 ±0.017
50.74	11.16 ± 0.11	0.829 ±0.017
53.26	9.043± 0.094	0.754 ±0.016
55.79	5.973± 0.066	0.612 ±0.017
58.31	3.674± 0.042	0.567 ±0.017
60.84	2.238± 0.025	0.549 ±0.017
63.35	1.767± 0.022	0.674 ±0.019
65.87	1.673± 0.018	0.859 ±0.017
68.39	1.636± 0.022	0.913 ±0.019
70.91	1.526± 0.021	0.935 ±0.020

^{89}Y

Angle	Cross Section (mb/sr)	Analyzing Power
13.26	4122.7 ±15.6	−0.0613±0.0055
14.27	2807.8 ± 9.1	−0.1003±0.0049
16.29	1110.4 ± 4.7	−0.2280±0.0066
18.32	286.2 ± 1.5	−0.5168±0.0092
18.82	183.4 ± 1.2	−0.617 ±0.011
19.33	113.6 ± 0.91	−0.685 ±0.013
19.83	67.61 ± 0.71	−0.699 ±0.018
20.34	45.18 ± 0.67	−0.410 ±0.021
21.35	42.17 ± 0.56	0.729 ±0.019
21.85	57.55 ± 0.75	0.892 ±0.019
22.36	79.28 ± 1.08	0.881 ±0.019
22.87	103.49 ± 1.01	0.796 ±0.015
23.37	129.67 ± 1.12	0.736 ±0.014
24.38	184.10 ± 1.64	0.554 ±0.014
26.40	247.47 ± 2.70	0.360 ±0.016
28.43	244.15 ± 2.19	0.256 ±0.013
30.35	197.56 ± 0.45	0.1805±0.0037
32.37	133.61 ± 1.17	0.061 ±0.012
34.39	69.24 ± 0.54	−0.0196±0.0098
36.41	32.32 ± 0.58	−0.085 ±0.025
36.51	28.40 ± 0.32	−0.045 ±0.016
38.43	15.34 ± 0.25	0.430 ±0.021
38.53	15.03 ± 0.23	0.470 ±0.022
40.45	15.91 ± 0.18	0.927 ±0.019
40.55	16.03 ± 0.22	0.965 ±0.019
42.46	21.20 ± 0.32	0.905 ±0.020
44.48	25.37 ± 0.33	0.770 ±0.018
45.49	25.81 ± 0.11	0.7165±0.0095
46.50	24.96 ± 0.33	0.639 ±0.017
48.52	20.94 ± 0.29	0.517 ±0.018
50.53	14.51 ± 0.11	0.4237±0.0096
54.56	5.60 ± 0.11	0.309 ±0.023
58.59	3.523± 0.084	0.852 ±0.031
62.61	3.826± 0.063	0.971 ±0.023

^{90}Zr

Angle	Cross Section (mb/sr)	Analyzing Power
13.26	3635.4 ±0.98	−0.0578±0.0040
14.27	2515.2 ±8.19	−0.1079±0.0050
16.29	995.3 ±5.2	−0.2324±0.0084
18.31	260.2 ±1.3	−0.4985±0.0093
19.32	101.12 ±0.82	−0.719 ±0.014
20.34	37.54 ±0.45	−0.435 ±0.017
21.35	35.44 ±0.69	0.752 ±0.026
22.36	69.61 ±0.96	0.883 ±0.021
23.37	117.37 ±1.03	0.723 ±0.015
24.38	163.27 ±1.48	0.562 ±0.015
26.40	223.64 ±1.73	0.396 ±0.012
28.42	216.17 ±1.38	0.2610±0.0098
30.34	176.68 ±0.25	0.1577±0.0023
32.36	112.62 ±0.21	0.0516±0.0030
34.38	58.22 ±0.15	0.0506..0.0040
36.40	25.72 ±0.11	0.0132±0.0050
38.42	13.877±0.084	0.5017±0.0087
40.44	15.040±0.084	0.955 ±0.012
42.46	20.08 ±0.19	0.891 ±0.014
44.48	23.20 ±0.21	0.759 ±0.013
46.49	23.26 ±0.44	0.576 ±0.012
46.49	21.68 ±0.29	0.617 ±0.012
50.53	12.40 ±0.37	0.376 ±0.016
54.56	4.572±0.105	0.310 ±0.027
58.58	3.219±0.084	0.880 ±0.026
62.61	3.564±0.084	0.956 ±0.026

^{98}Mo

Angle	Cross Section (mb/sr)	Analyzing Power
14.15	2511.0 ±16.1	−0.1106±0.0095
16.17	906.8 ± 6.8	−0.274 ±0.011
18.20	188.1 ± 1.5	−0.616 ±0.013
19.21	59.19 ± 0.78	−0.816 ±0.019
20.22	32.70 ± 0.75	0.316 ±0.026
22.24	118.48 ± 1.16	0.753 ±0.015
24.26	228.59 ± 1.98	0.491 ±0.013
26.28	264.20 ± 2.60	0.301 ±0.015
26.78	266.60 ± 2.34	0.266 ±0.013
28.80	220.98 ± 2.13	0.181 ±0.014
30.32	164.74 ± 1.09	0.0958±0.0098
32.84	76.25 ± 0.45	−0.0619±0.0087
33.85	50.49 ± 0.37	−0.095 ±0.011
35.36	25.46 ± 0.33	−0.035 ±0.019
36.37	16.80 ± 0.21	0.137 ±0.019
37.88	13.00 ± 0.19	0.730 ±0.020
39.40	16.21 ± 0.21	0.939 ±0.018
40.40	18.97 ± 0.20	0.941 ±0.016
42.93	25.01 ± 0.23	0.720 ±0.014
45.45	23.56 ± 0.23	0.55 ±0.015
47.96	16.02 ± 0.19	0.429 ±0.017
50.48	8.921± 0.099	0.271 ±0.016
53.00	4.397± 0.069	0.324 ±0.023
55.52	2.982± 0.051	0.665 ±0.023
58.03	3.140± 0.052	0.976 ±0.021
60.54	3.348± 0.049	0.959 ±0.019
63.06	3.082± 0.047	0.901 ±0.020
65.57	2.242± 0.040	0.793 ±0.024
68.08	1.364± 0.031	0.717 ±0.030
70.59	0.834± 0.025	0.497 ±0.041

^{100}Mo

Angle	Cross Section (mb/sr)	Analyzing Power
14.15	2863.1 ±26.9	−0.110±0.015
16.17	974.9 ± 9.1	−0.335±0.015
18.19	183.7 ± 2.2	−0.695±0.018
19.20	57.55 ± 0.86	−0.778±0.022
20.21	40.82 ± 0.41	0.603±0.016
21.22	86.52 ± 1.05	0.886±0.018
22.23	153.96 ± 1.56	0.697±0.016
24.25	278.85 ± 2.43	0.444±0.014
26.27	315.50 ± 2.37	0.311±0.012
26.27	315.14 ± 2.82	0.294±0.014
27.79	284.24 ± 2.74	0.232±0.015
28.29	270.79 ± 2.39	0.201±0.014
30.31	179.64 ± 1.78	0.076±0.016
32.83	78.22 ± 0.84	−0.079±0.017
34.35	40.63 ± 0.43	−0.170±0.017
35.35	25.16 ± 0.26	−0.058±0.016
36.36	17.49 ± 0.22	0.237±0.020
37.88	15.32 ± 0.19	0.814±0.019
39.39	19.43 ± 0.22	0.947±0.018
40.40	23.18 ± 0.25	0.921±0.017
42.92	29.53 ± 0.34	0.708±0.018
45.44	25.96 ± 0.26	0.535±0.016
50.47	8.918 ± 0.109	0.256±0.019
55.51	3.459 ± 0.068	0.776±0.026

^{144}Sm

Angle	Cross Section (mb/sr)	Analyzing Power
13.60	4245.2 ±18.5	−0.1488±0.0069
14.10	3283.5 ±16.3	−0.1895±0.0077
15.11	1728.1 ±11.8	−0.270 ±0.011
16.12	800.9 ± 5.7	−0.416 ±0.012
17.13	315.8 ± 2.5	−0.541 ±0.013
18.13	146.0 ± 1.3	−0.100 ±0.013
19.14	172.3 ± 1.5	0.530 ±0.014
19.64	214.1 ± 2.4	0.588 ±0.016
20.15	282.0 ± 2.4	0.580 ±0.014
21.15	406.4 ± 3.3	0.454 ±0.013
22.16	502.3 ± 3.2	0.367 ±0.010
23.17	562.4 ± 4.8	0.278 ±0.013
24.17	549.7 ± 4.7	0.192 ±0.013
25.18	524.4 ± 4.6	0.127 ±0.013
26.19	444.3 ± 3.5	0.064 ±0.012
27.20	351.3 ± 3.8	−0.024 ±0.016
28.20	263.2 ± 1.9	−0.110 ±0.010
29.21	177.3 ± 1.5	−0.213 ±0.013
30.21	107.86 ± 0.82	−0.340 ±0.012
31.22	58.02 ± 0.50	−0.508 ±0.013
31.72	41.69 ± 0.38	−0.566 ±0.014
32.23	29.55 ± 0.36	−0.546 ±0.018
33.23	17.08 ± 0.19	−0.061 ±0.016
34.24	17.60 ± 0.25	0.779 ±0.020
35.25	25.74 ± 0.23	0.990 ±0.015
36.25	37.06 ± 0.45	0.889 ±0.017
38.26	56.53 ± 0.55	0.645 ±0.015
40.28	59.73 ± 0.31	0.4482±0.0089
42.29	46.77 ± 0.28	0.2746±0.0093
43.79	34.05 ± 0.24	0.137 ±0.010
44.30	29.10 ± 0.18	0.0826±0.0091
46.31	14.57 ± 0.13	−0.110 ±0.013
47.31	9.816± 0.091	−0.151 ±0.014
48.32	6.837± 0.087	0.015 ±0.019

^{144}Sm (continued)

Angle	Cross Section (mb/sr)	Analyzing Power
49.32	5.866± 0.081	0.385 ±0.020
50.33	5.998± 0.071	0.707 ±0.017
51.33	6.789± 0.075	0.945 ±0.017
52.34	7.992± 0.082	0.981 ±0.016
54.35	9.695± 0.090	0.909 ±0.015
56.35	9.564± 0.080	0.767 ±0.014
58.36	7.601± 0.071	0.640 ±0.014
60.37	5.111± 0.059	0.433 ±0.017
62.38	3.043± 0.036	0.294 ±0.020
64.38	1.931± 0.033	0.270 ±0.027
66.39	1.699± 0.027	0.556 ±0.022
68.40	1.904± 0.023	0.899 ±0.017
70.40	2.086± 0.024	0.971 ±0.017
72.41	1.972± 0.024	0.978 ±0.017
74.41	1.701± 0.022	0.965 ±0.018

^{208}Pb

Angle	Cross Section (mb/sr)	Analyzing Power
13.17	6644.7 ±9.3	−0.1224±0.0027
14.17	3484.6 ±6.8	−0.1648±0.0037
15.18	1795.0 ±4.9	−0.1426±0.0044
16.18	1034.3 ±3.7	0.0025±0.0052
17.19	884.0 ±3.4	0.2444±0.0066
18.19	966.9 ±3.6	0.3079±0.0068
19.20	1116.9 ±3.8	0.2867±0.0064
20.20	1222.1 ±4.0	0.2325±0.0057
21.21	1207.0 ±4.0	0.1639±0.0053
22.21	1106.3 ±3.8	0.0910±0.0051
23.22	929.8 ±3.5	0.0166±0.0054
24.22	709.2 ±3.0	−0.0590±0.0062
25.23	492.3 ±1.8	−0.1751±0.0057
26.23	301.2 ±1.4	−0.3384±0.0081
27.24	156.8 ±1.0	−0.531 ±0.011
28.24	66.59 ±0.47	−0.850 ±0.013
28.74	43.14 ±0.38	−0.925 ±0.015
29.24	30.01 ±0.31	−0.727 ±0.016
30.25	28.36 ±0.31	0.502 ±0.016
30.75	37.42 ±0.31	0.762 ±0.014
31.25	51.92 ±0.37	0.831 ±0.013
31.76	66.78 ±0.66	0.811 ±0.016
32.26	80.25 ±0.46	0.741 ±0.013
32.76	99.68 ±0.93	0.693 ±0.015
34.27	128.36 ±0.71	0.484 ±0.010
36.27	127.52 ±0.71	0.2794±0.0088
38.28	87.84 ±0.59	0.051 ±0.010
39.29	63.59 ±0.50	−0.083 ±0.011
40.29	43.00 ±0.41	−0.264 ±0.015
41.29	24.33 ±0.22	−0.462 ±0.013
42.30	13.55 ±0.15	−0.577 ±0.017
43.30	8.479±0.130	−0.313 ±0.022
44.31	8.113±0.090	0.488 ±0.016
45.31	11.192±0.122	0.912 ±0.016
46.31	15.921±0.159	0.958 ±0.017
47.32	19.987±0.199	0.872 ±0.016
48.32	22.723±0.212	0.750 ±0.016
50.33	23.864±0.218	0.569 ±0.015
52.33	17.468±0.167	0.333 ±0.014
54.34	10.042±0.142	0.0082±0.205
55.34	6.627±0.081	−0.145 ±0.018
56.35	4.505±0.060	−0.265 ±0.019
57.35	3.202±0.056	−0.134 ±0.026
58.35	2.992±0.055	0.178 ±0.026
60.36	3.705±0.061	0.856 ±0.021
61.36	4.463±0.067	0.960 ±0.020
62.36	4.926±0.070	0.974 ±0.019
64.37	5.272±0.092	0.875 ±0.022
66.37	4.325±0.066	0.660 ±0.022
68.38	2.814±0.047	0.468 ±0.024
70.38	1.516±0.035	0.212 ±0.033

^{209}Bi

Angle	Cross Section (mb/sr)	Analyzing Power
13.33	6329.9 ±12.3	−0.1249±0.0033
14.34	3364.9 ± 8.9	−0.1646±0.0045
14.84	2462.5 ± 7.6	−0.1613±0.0051
15.18	1950.7 ± 6.8	−0.1591±0.0052
15.34	1776.9 ± 6.5	−0.1482±0.0057
15.85	1272.9 ± 5.5	−0.0955±0.0064
16.18	1088.5 ± 3.6	−0.0302±0.0045
16.35	1034.6 ± 4.9	0.0084±0.0070
16.68	913.0 ± 3.3	0.0779±0.0050
17.19	845.0 ± 3.2	0.1971±0.0057
17.35	851.8 ± 4.5	0.2250±0.0083
17.69	853.8 ± 3.2	0.2905±0.0063
18.19	896.9 ± 3.3	0.3066±0.0061
18.69	969.6 ± 3.4	0.3071±0.0061
19.20	1036.1 ± 3.5	0.2950±0.0058
20.20	1138.3 ± 3.7	0.2468±0.0054
20.37	1170.5 ± 5.3	0.2320±0.0073
22.21	1068.2 ± 3.6	0.1070±0.0049
24.22	701.1 ± 1.4	−0.0552±0.0030
26.23	309.08 ± 0.96	−0.3173±0.0056
27.40	148.84 ± 1.19	−0.560 ±0.013
28.24	75.20 ± 0.39	−0.811 ±0.011
28.91	41.52 ± 0.57	−0.908 ±0.019
29.24	31.28 ± 0.25	−0.832 ±0.013
30.25	25.17 ± 0.22	0.271 ±0.013
30.41	27.32 ± 0.51	0.433 ±0.027
30.92	35.72 ± 0.46	0.806 ±0.019
31.42	48.72 ± 0.48	0.819 ±0.015
31.92	64.34 ± 0.62	0.797 ±0.015
32.76	88.27 ± 0.21	0.6865±0.0084
35.27	128.16 ± 0.36	0.3931±0.0059
35.43	131.64 ± 1.11	0.379 ±0.013
37.78	98.34 ± 0.70	0.1175±0.0098
41.96	17.60 ± 0.22	−0.593 ±0.018
42.46	13.32 ± 0.20	−0.659 ±0.021
42.80	11.09 ± 0.13	−0.546 ±0.017
43.47	8.146± 0.152	−0.295 ±0.027
44.30	7.855± 0.138	0.386 ±0.024
45.31	10.471± 0.101	0.857 ±0.014
46.48	15.32 ± 0.21	0.931 ±0.019
47.82	20.39 ± 0.22	0.833 ±0.016
50.33	23.19 ± 0.17	0.557 ±0.011
52.83	15.54 ± 0.16	0.276 ±0.014
55.34	6.922± 0.083	−0.145 ±0.017
56.51	4.374± 0.091	−0.288 ±0.030
57.85	2.965± 0.032	−0.043 ±0.015
60.36	2.628± 0.060	0.849 ±0.021
61.52	4.388± 0.083	0.952 ±0.023
62.86	4.943± 0.078	0.935 ±0.020
65.37	4.773± 0.058	0.813 ±0.016
67.87	3.065± 0.050	0.506 ±0.022
70.38	1.531± 0.031	0.104 ±0.028
72.88	0.935± 0.018	0.136 ±0.027
75.38	1.082± 0.016	0.667 ±0.020

REFERENCES

1) J. P. Jeukenne, A. Lejeune and C. Mahaux, Phys. Rev. **C10** (1974), 1391.
2) J. P. Jeukenne, A. Lejeune and C. Mahaux, Phys. Rep. **25C** (1976), 83.
3) J. P. Jeukenne, A. Lejeune and C. Mahaux, Phys. Rev. **C15** (1977), 10.
4) J. P. Jeukenne, A. Lejeune and C. Mahaux, Phys. Rev. **C16** (1977), 80.
5) F. A. Brieva and J. R. Rook, Nucl. Phys. **A291** (1977), 299.
6) F. A. Brieva and J. R. Rook, Nucl. Phys. **A291** (1977), 377.
7) F. A. Brieva and J. R. Rook, Nucl. Phys. **A297** (1978), 206.
8) F. A. Brieva and J. R. Rook, Nucl. Phys. **A307** (1978), 493.
9) F. A. Brieva, Phys. Lett. **76B** (1978), 533.
10) C. W. Wong, Nucl. Phys. **A91** (1967), 399.
11) J. W. Negele, Phys. Rev. **C1** (1970), 1260.
12) F. D. Becchetti and G. W. Greenlees, Phys. Rev. **182** (1969), 1190.
13) E. Fabrici, S. Micheletti, M. Pignanelli, F. G. Resmini, R. DeLeo, G. D'Erasmo, A. Pantaleo, J. L. Escudie and A. Tarrats, Phys. Rev. **C21** (1980), 830.
14) E. Fabrici, S. Micheletti, M. Pignanelli, F. G. Resmini, R. DeLeo, G. D'Erasmo and A. Pantaleo, Phys. Rev. **C21** (1980), 844.
15) H. O. Meyer, P. Schwandt, G. L. Moake, P. P. Singh, Phys. Rev. **C23** (1981), 616.
16) A. Nadasen, P. Schwandt, P. P. Singh, W. W. Jacobs, A. D. Bacher, P. T. Debevec, M. D. Kaitchuck and J. T. Meek, Phys. Rev. **C23** (1981), 1023.
17) L. G. Arnold, B. C. Clark, R. L. Mercer, P. Schwandt, Phys. Rev. **C23** (1981), 1949.
18) H. Sakaguchi, M. Nakamura, K. Hatanaka, A. Goto, T. Noro, F. Ohtani, H. Sakamoto and S. Kobayashi, Phys. Lett. **89B** (1979), 152.
19) H. Sakaguchi, M. Nakamura, K. Hatanaka, T. Noro, F. Ohtani, H. Sakamoto, H. Ogawa and S. Kobayashi, Phys. Lett. **99B** (1981), 92.
20) T. Noro, H. Sakaguchi, M. Nakamura, K. Hatanaka, F. Ohtani, H. Sakamoto and S. Kobayashi, Nucl. Phys. **A366** (1981), 189.
21) K. Imai, N. Tamura and K. Nisimura, RCNP Annual Report (1976), p. 23.
22) M. Kondo et al., Proc. of 7-th Int. Conf. on Cyclotron and their Applications (Birkhauser, Basel, 1975), p. 95.
23) N. Matsuoka, K. Hosono, T. Saito, A. Shimizu and M. Kondo, RCNP Annual Report (1976), p. 97.
24) K. Imai, K. Hatanaka, H. Shimizu and K. Nisimura, RCNP Annual Report (1978), p. 154.
25) S. Kato, K. Okada, M. Kondo, A. Shimizu, K. Hosono, T. Saito, N. Matsuoka, S. Nagamachi, K. Nisimura, N. Tamura, K. Imai, K. Egawa, M. Nakamura, T. Noro, H. Shimizu, K. Ogino, Y. Kadota, Nucl. Instr. & Meth. **169** (1980), 589.
26) M. Q. Makino, C. N. Waddell and R. M. Eisberg, Nucl. Instr. & Meth. **60** (1968), 109.
27) J. Raynal, Saclay, Code MAGALI.
28) G. W. Greenlees, G. J. Pyle and Y. C. Tang, Phys. Rev. **C171** (1968), 1115.
29) L. R. B. Elton, Nuclear Sizes, (Oxford Univ. Press, Oxford, 1961), p. 107.
30) B. Sinha, Phys. Lett. **20C** (1975), 1.
31) R. C. Barrett and D. F. Jackson, Nuclear Sizes and Structure (Clarendon Press, Oxford, 1977), p. 146.
32) C. M. Perey and F. G. Perey, Atomic Data and Nucl. Data Tables **13** (1974), 293.
33) J. A. Nolen Jr. and J. P. Schiffer, Phys. Lett. **29B** (1969), 396.
34) S. Shlomo and E. Friedman, Phys. Rev. Lett. **39** (1977), 1180.
35) G. D. Alkhazov, S. L. Belostotsky, O. A. Domchenkov, Yu. V. Dotsenko, N. P. Kuropatkin, M. A. Schuvaev and A. A. Vorobyov, Phys. Lett. **57B** (1975), 47.
36) G. D. Alkhazov, T. Bauer, R. Bertini, L. Bimbot, O. Bing, A. Boudard, G. Bruge, H. Catz, A. Chaumeaux, P. Couvert, J. M. Fontaine, F. Hibou, G. J. Igo, J. C. Lugol and M. Matoba, Nucl. Phys. **A280** (1977), 365.
37) G. C. Alkhazov, T. Bauer, R. Beurtey, A. Boudarad, G. Bruge, A. Chaumeaux, P. Couvert, G. Cvijanovich, H. H. Duhm, J. M. Fontaine, J. C. Lugol, J. Saudinos, J. Thirion and

A. A. Vorobyov, Nucl. Phys. **A274** (1974), 443.
38) G. W. Hoffman, G. S. Blannpied, W. R. Coker, R. P. Liljestrand, N. M. Hintz, M. A. Oothoudt, T. S. Bauer, G. Igo, G. Pauletta, J. Soukup, C. A. Whitten Jr., D. Madland, J. C. Pratt, L. Ray, J. E. Spencer, H. A. Thiessen, H. Nann, K. K. Seth, C. Glashausser, D. K. McDaniels, J. Tinsley and P. Varghesse, Phys. Rev. Lett. **40** (1978), 1256.
39) G. W. Hoffman et al., Phys. Lett. **76B** (1978), 383.
40) G. W. Hoffman et al., Phys. Lett. **79B** (1978), 376.
41) G. Igo et al., Phys. Lett. **81B** (1979), 151.
42) L. Ray, G. W. Hoffman, G. S. Blanpied, W. R. Doker and R. P. Liljestrand, Phys. Rev. **C18** (1978), 1757.
43) L. Ray, W. R. Coker, G. W. Hoffmann, Phys. Rev. **C18** (1978), 2641.
44) G. Bertsch, J. Borysowicz and H. McManus, Nucl. Phys. **A284** (1977), 399.
45) K. Hatanaka, K. Imai, S. Kobayashi, T. Matsusue, M. Nakamura, K. Nishimura, T. Noro, H. Sakamoto, H. Shimizu and J. Shirai, Nucl. Phys. **A340** (1980), 93.
46) M. Hyakutake, M. Matoba, I. Kumabe, M. Fukada, T. Komatsuzaki, T. Yamagata, M. Tanaka, M. Inoue, I. Miura, and H. Ogata, Nucl. Phys. **A311** (1978), 161.
47) A. Lejeune and P. E. Hodgson, Nucl. Phys. **A295** (1978), 301.
48) F. A. Brieva, in Microscopic Optical Potential, ed. H. V. v. Geramb, Lecture Notes in Physics 89 (Springer-Verlag, Berlin Heidelberg New New Yourk 1979) p. 84.